Ng, F.S.L, Barr, I.D. and Clark, C.D. (2010) Using the surface profiles of modern ice masses to inform palaeo-glacier reconstructions. *Quaternary Science Reviews*, 29(23-24), 3240-3255. doi:10.1016/j.quascirev.2010.06.045 [Corresponding author email addr: f.ng@sheffield.ac.uk]

Using the surface profiles of modern ice masses to inform palaeo-glacier reconstructions

revised version

Felix S.L. Ng, Iestyn D. Barr, & Chris D. Clark
Department of Geography, University of Sheffield, Winter Street, Sheffield, S10 2TN, UK

Abstract

Morphometric study of modern ice masses is useful because many reconstructions of glaciers traditionally draw on their shape for guidance. Here we analyse data derived from the surface profiles of 200 modern ice masses—valley glaciers, icefields, ice caps, and ice sheets with length scales from 10^0 to 10^3 km—from different parts of the world. Four profile-attributes are investigated: relief, span, and two parameters C^* and $\tilde{C}$ that result from using Nye's (1952) theoretical parabola as a profile descriptor. C^* and $\tilde{C}$ respectively measure each profile's aspect ratio and steepness, and are found to decrease in size and variability with span. This dependence quantifies the competing influences of unconstrained spreading behaviour of ice flow and bed topography on the profile shape of ice masses, which becomes more parabolic as span increases (with C^* and $\tilde{C}$ tending to low values of 2.5–3.3 $m^{1/2}$). The same data reveal coherent minimum bounds in C^* and $\tilde{C}$ for modern ice masses that we develop into two new methods of palaeo-glacier reconstruction. In the first method, glacial limits are known from moraines, and the bounds are used to constrain the lowest palaeo ice surface consistent with modern profiles. We give an example of applying this method over a three-dimensional glacial landscape in Kamchatka. In the second method, we test the plausibility of existing reconstructions by comparing their C^* and $\tilde{C}$ against the modern minimum bounds. Of the 86 published palaeo ice masses that we put to this test, 88% are found to be plausible. The search for other morphometric constraints will help us formalise glacier reconstructions and reduce their uncertainty and subjectiveness.

1. Introduction

The evolving configurations of past glaciers and ice sheets played a key role in the Earth's Quaternary environmental history, and various methods have been used to reconstruct them from the landform record (see: Andrews, 1982; Kleman and Borgström, 1996). In these reconstructions, a common goal is to deduce the three-dimensional shape of an ice mass to gauge its volume and sea-level impact (Clark and Mix, 2000). Another goal is to estimate its equilibrium line altitude (ELA), and hence infer past climatic conditions (Sissons and Sutherland, 1976; Sutherland, 1984; Porter, 2001; Ballantyne, 2007a). Such inferences may be studied on a regional scale (e.g. Ballantyne, 1989; Stansell et al., 2007) and alongside other palaeo-environmental datasets (e.g. Mark et al., 2005); if extensive, they may also be used to test general circulation models (Allen et al., 2008).

There have been numerous debates and developments on how best to estimate the ELA of palaeoglaciers from their surface topography (e.g. Meierding, 1982; Porter, 2001; Kaser and Osmaston, 2002; Benn et al. 2005; Osmaston, 2005). It is recognised, for instance, that a glaciologically-sensible method should account for the elevation dependence of glacier area, i.e., glacier hypsometry (Benn and Gemmell, 1997; Porter, 2001; Kaser and Osmaston, 2002; Osmaston, 2005) and that this consideration is missing from the classic Accumulation-Area-Ratio method (Meier and Post, 1962) adopted by some studies (e.g. Balascio et al., 2005). However, the process of reconstructing the palaeo ice surface itself from geomorphological evidence is deeply uncertain, so that reconstructed topography could seriously misrepresent the palaeo ice masses. The lack of a definitive methodology in this inverse problem is well known (Sugden and John, 1976; Golledge and Hubbard, 2005) and is what motivates the present study.

Given the margins of a palaeo ice mass at a certain time (e.g. delineated by moraines of a known age) and its bed topography, where was its surface and how thick was the ice? When additional clues from trimlines are absent (as in many accumulation zones), reconstructing the surface essentially involves extrapolation from the margins.

Published reconstructions usually take one of two approaches. On the one hand, many researchers have traditionally produced hand-drawn contour maps of palaeo ice surfaces (e.g. Fig. 1a) based on intuitions gained from the morphology of glaciers today (e.g. Sissons, 1980; Ballantyne, 1989; Benn and Ballantyne, 2005). This approach relies heavily on geomorphological evidence and not explicitly on glacier physics, and the

results depend on the practitioner's skill—subjective notions and experience of what glaciers *should* look like. On the other hand, numerical models formulated from physics are now routinely used (e.g. Boulton and Hagdorn, 2006; Hubbard et al., 2006; Golledge et al., 2008) to stimulate three-dimensional ice masses (e.g. Fig. 1b) that evolve in time and respect geomorphological evidence. These models' sophistication does not guarantee robust results, because some of their ingredients are debated (e.g. basal sliding law, anisotropy in ice rheology) and not all model parameters can be well constrained (e.g. palaeoclimate). Consequently, the two approaches continue to occupy their niche in the literature, although recent studies have used them together to improve the reliability of reconstructions (e.g. Golledge and Hubbard, 2005).

The hand-drawing approach treats modern ice masses as *analogues* of palaeo ice masses, but this assumption is implicated also in the numerical approach, because models are inherently tuned to fit modern observations prior to their use in reconstructions. As modern ice masses inform both approaches, a morphometric analysis of them should prove beneficial; here we investigate this avenue. At least, the results may help practitioners of the former approach to formalise their methods.

The specific idea is this: We assume that the surfaces of palaeo and modern ice masses have similar *shape*, and we measure the shape of modern ice masses to generate empirical data for guiding the reconstruction of palaeo ice surfaces. Various shape properties (e.g. slope, curvature) may be studied; for simplicity we explore those of surface profiles traced along the ice-flow direction.

To our knowledge, a systematic analysis has not previously been made of the surface profiles of large samples of ice masses. In the following, Section 2 details the framework of our analysis, and Section 3 describes our data compilation, which involves selecting contemporary ice masses from satellite images, retrieving their topography from digital elevation models (DEMs), and sampling surface profiles from these DEMs. We record also the 'glaciation style' or 'morphological type' of each ice mass: whether it is classified as *valley glacier*, *icefield*, *ice cap*, or *ice sheet*. Interesting attributes of each profile include relief, length, and parameters measuring steepness and convexity (C^* and $\tilde{C}$ introduced below). We diagnose trends among these in Section 4. It turns out that modern ice masses exhibit clear lower limits in the two 'C-values', allowing us to constrain the palaeo ice surface and glaciation style in reconstructions. Using this result,

in Section 5 we develop a 'minimum reconstruction' tool and illustrate it through a case study in Kamchatka, far-eastern Siberia and by evaluating previously published glacial reconstructions. Conclusions and outlook are given in Section 6.

2. A parametric model of ice-surface profiles

The spreading motion of ice over land—thus an ice mass's morphology—depends on its internal property (ice rheology), inputs and outputs (mass balance, governed by climate via accumulation and ablation), bed topography, and basal sliding conditions. Formal calculation of the ice surface requires solving the fluid mechanics of the ice flow, and even for the situation along flowlines this could be done using a hierarchy of models. At the complicated end are models consisting of the 'full' Stokes equations (Paterson, 1994; p. 258-262), while popular until recently have been simplified versions of these equations based on the shallow-ice approximation (Hutter, 1983; Fowler, 1992). Still simpler models exist. In the following analysis we adopt one of the simplest models, due to Nye (1951, 1952).

Our focus is not the ice-flow problem but the use of this classical model to fit observed surface profiles to yield a *parametric description* of them. Many profiles will be used to enable an extensive empirical analysis of modern ice masses, which has not been done before. Nye's model is also used to estimate palaeo ice surfaces in the later part of the paper. Although any ice mass may be studied in these ways, model assumptions can limit their validity and how we interpret the results. We elaborate on our choice of Nye's model in relation to this after first outlining its formulation.

Nye's (1951, 1952) model describes the cross-sectional profile of an ice mass lying on a horizontal bed. To capture the flow mechanics, it assumes that force gradients resulting from the surface slope of each vertical ice section are balanced by a constant basal shear stress τ_0, which may be interpreted as the yield stress for flow to occur. Under this perfect-plasticity assumption, τ_0 equals the driving stress, $\rho g h(\mathrm{d}h/\mathrm{d}x)$, where h is ice surface elevation, ρ is ice density, g is gravitational acceleration, and x is horizontal distance from the ice margin in the up-glacier direction. Solving the equation $\tau_0 = \rho g h(\mathrm{d}h/\mathrm{d}x)$ for h gives the parabolic ice-surface profile

$$h(x) = C\sqrt{x}\,, \qquad (1)$$

where the constant is

$$C = \left(\frac{2\tau_0}{\rho g} \right)^{\frac{1}{2}}. \qquad (2)$$

Fig. 2a shows this theoretical profile and our coordinate system. We denote by H the *relief* of the profile (difference between maximum and minimum elevations), and by L its length or *span* (for a symmetric ice sheet or cap this is halfway across). The parameter C describes the overall 'stiffness' of the flow (encapsulating ice viscosity and basal resistance) and can be found by fitting Eqn. (1) to the surface profile of a given ice mass. For example, Nye (1951) examined one east-west profile across the Greenland Ice Sheet and found $C \approx 4.8$ m$^{1/2}$, which corresponds to $\tau_0 \approx 10^5$ Pa.

We propose to fit Eqn. (1) to modern ice masses to find their H, L and C and look for trends among these morphological parameters. We then direct insights from this toward glacier reconstruction. Notably, if the data suggest a fixed C-value for specific ice masses, then we can use it in Eqn. (1) to back-extrapolate palaeo ice surfaces from terminal moraines; how such surface intersects with the three-dimensional bed also indicates the glaciation style. Theoretical profiles have been used before to recreate the Last Glacial Maximum ice sheets (Sugden, 1977; Hughes, 1981; Reeh, 1982).

The Nye model has a well-known limitation that its assumption of a flat bed breaks down at short length scales where basal topography can influence the ice flow and surface topography strongly (Van der Veen, 1999; p. 149). This restricts its application to large ice masses, whereas for small ice masses a variant of it, called the 'flowline model', needs to be used. Like Nye's model, the flowline model is independent of time, assumes perfect plasticity, and predicts an infinite slope at $x = 0$ (thus does not capture the shape of real ice margins); however, it improves on the Nye model by accounting for the bed topography $b(x)$ so that the stress balance becomes $\tau_0 = \rho g(h–b)\mathrm{d}h/\mathrm{d}x$. Given $b(x)$ and the basal shear stress τ_0, this equation can be solved for the palaeo ice surface by a numerical integration scheme that marches back from the margin (Schilling and Hollin, 1981), and a user-friendly computer implementation of this scheme (as an Excel spreadsheet) has recently been given by Benn and Hulton (2010). The flowline model may be used to reconstruct ice masses of any size; examples of this appear in the work of Locke (1995), Fredin (2004), and Rea and Evans (2007).

Despite this, we have reasons to prefer the Nye model over the flowline model here. Crucially, our proposed analysis requires fitting either model to ice masses to extract τ_0 or C, but this cannot be done with the flowline model unless $b(x)$ is known, and modern ice masses whose bed topography have been determined by radar sounding or other techniques are too few to enable a sufficient study. (While more measurements may allow the flowline model to be used, we leave this for future research.) The Nye model, on the other hand, requires only the ice surface to be known. Note that when using it to measure profile characteristics below, we are not claiming that real ice surfaces are parabolic.

A second reason is that Eqn. (1) is already popular in the palaeoglaciological literature for checking the reconstructed shape of ice caps and ice sheets (e.g. Ballantyne et al., 2008). We introduce a new way of doing this in Section 5.3.

A further reason derives from the Nye-model results—on hindsight. As we shall see, C varies substantially between modern ice masses so in fact there is no unique C-value in Eqn. (1) for reconstructing surface profiles directly (Section 4.3). But modern C-values may be used to deduce a profile that represents the lowest palaeo ice surface consistent with modern observations (Section 5.1). In this context, the Nye model acts as a purely parametric device and its limitation does not matter. Physically, though, the fact that C reflects flow 'stiffness' suggests that it could be interpreted (crudely) for factors like ice viscosity and basal resistance, and indeed we will analyse variations in our C-value data for such controls. In this context the model limitation does matter: we bear in mind that the smaller is an ice mass, the more likely might basal topography corrupt its C-value, and the more uncertain will be the physical interpretation.

3. Data compilation

3.1. Surface profiles of modern ice masses

We have extracted surface profiles from 200 ice masses ranging in scale from small glaciers ($L \sim 10^0$ km) to continental ice sheets ($L \sim 10^3$ km). Table 1 lists these ice masses and Fig. 3 locates them on a global map. Ice streams and known surging glaciers are excluded. Although it is impractical for us to include all ice masses on Earth today, our samples cover a broad range of latitudes, climatic and elevation zones, and polar and mountain environments. In fact, since we are more interested in the *variety* of the morphology of ice masses than their average shape, our chief concern is not whether each

ice mass is regionally representative, but the number of samples in our dataset. We believe our sample size to be adequate for the purpose here because certain *envelopes* of our data (Section 4) seem to be stable. Worldwide glacier recession may introduce a bias on the shape of modern surface profiles that affects their use in palaeo reconstructions; we discuss this caveat alongside the assumption of modern analogues in Section 5.

For each ice mass, we first used Landsat ETM+ satellite imagery (15-m resolution) to identify its margin, and as mentioned before we classified it morphologically as a *valley glacier*, *icefield*, *ice cap*, or *ice sheet*. This was done according to published definitions in the World Glacier Inventory (National Snow and Ice Data Center, 1999); where inventory data of the ice mass is lacking, we relied on our own interpretation of the Landsat imagery. Next we retrieved digital elevations of the area, by using 90-m resolution data from the Shuttle Radar Topography Mission (SRTM) if the area lies between 60ºN and 56ºS, or by using 1-km resolution Global Topographic Data (GTOPO30) if it lies above 60ºN or below 56ºS. The low resolution of the latter data is sufficient because our polar ice masses have length scales much greater than 1 km. (The recently available ASTER Global Digital Elevation Map also suits this work, but our data collection had finished long before its release in June 2009.)

From the digital elevations, surface profiles (x, h data) were extracted along flowlines that we traced by following the direction of the maximum surface slope. The ice margin on each profile is used as the elevation datum and positioned at $x = 0$, $h = 0$. For each valley glacier, we measured 3 profiles from the snout as far as the valley headwall; and for each ice sheet, ice cap, or icefield we measured 10 profiles linking the ice margin to interior divides in different directions. Such sampling allows the calculation of mean shape parameters for each ice mass later. Our dataset includes 160 valley glaciers and 40 ice fields/caps/sheets, so a total of 880 surface profiles were measured.

3.2. Profile shape parameters

Because a typical real surface profile is not precisely parabolic, there are different choices of fitting Eqn. (1) to it. We employ two methods, each yielding a C-value that reflects a different aspect of the profile. The idea is illustrated in Fig. 2b.

The first method involves a two-point fit that uses (x, h) data at the ends of the profile only, i.e., the margin and its furthest (and highest) point. Thus we calculate

$$C^* = \frac{H}{\sqrt{L}} \qquad (3)$$

(following from Eqn. (1)), where L and H denote the profile's span and relief, as before. The parameter C^* may be thought of as an aspect ratio of the profile (similar in spirit to H/L, the mean slope) but has the unit $m^{1/2}$ and is therefore not dimensionless.

The second method 'best' fits Eqn. (1) to the entire surface profile by minimising vertical errors (in h) in a least-square sense, while forcing the fit through the ice margin. It yields a coefficient of determination, r^2, as well as the profile shape parameter, which we denote by $\tilde{C}$.

As Fig. 2b shows, we expect $\tilde{C}$ and C^* to have the same order of magnitude for a given surface profile. $\tilde{C}$ will be approximately equal to C^* for convex profiles that closely resemble a parabola, but much less than C^* for concave or less convex profiles. Note that neither the ice thickness nor the bed topography enters these calculations.

After performing these fits to all of the collected profiles, we gathered L, H, C^*, and $\tilde{C}$ for all profiles pertaining to each ice mass and averaged each parameter to form our dataset (this is listed in columns 6–9 of Table 1). From now on it is understood that these parameters describe the mean surface morphology of an ice mass.

4. Modern ice masses: morphometric analysis

We proceed to examine the H, L, C^*, and $\tilde{C}$ data (Table 1) for patterns that might reveal distinguished characteristics about the surface profiles of modern ice masses. In this section, our analysis leads us to discover empirical constraints on C^* and $\tilde{C}$, which we later fashion into a glacier-reconstruction tool in Section 5.

4.1. Relief and span

As reconstructions typically begin with knowledge of the distances between terminal moraines and inferred ice divides, we query how other parameters vary with the span L. Fig. 4 plots relief H against L, using different symbols for glaciers, icefields and ice sheets/caps. In roughly this order, these morphological types cover a continuum of length scales over three orders of magnitude. There are few large ice masses so the data thin out considerably at the high end of this range.

Not surprisingly, large ice masses have high relief, but a weak correlation between H and L precludes reliable reconstruction of palaeo surface relief from span. Despite this,

the data occupy a wedge emanating from the plot origin with tentative upper and lower boundaries (Fig. 4b). This suggests recasting them in some ratio involving powers of H and L, such as C^* (= $H/L^{0.5}$), and brings us to consider the C-values.

4.2. C-values and their latitudinal distribution

One could expect polar ice masses to be stiffer (have higher C) than equatorial ones because low surface temperatures favour cold, high-viscosity ice. However, complicating this argument are the ice thickness and velocity, which, through their effect on englacial heat transfer, influence whether an ice mass is temperate- or cold-based, thus whether basal sliding can occur. Coupled to this is also subglacial hydrology, and we will see that basal topography can affect the C-values. Regardless of the details, this consideration motivates a search for a latitudinal dependence of C^* and $\tilde{C}$.

We do this in Fig. 5, alongside the comparison of $\tilde{C}$ against C^* in Fig. 6 which shows that typically $C^* > \tilde{C}$ for all morphological types. Polar ice sheets and caps have almost equal C^* and $\tilde{C}$ for their near-parabolic surface profiles; in contrast, many low-latitude valley glaciers display large differences between C^* and $\tilde{C}$, reflecting more concave profiles. Although the data in Fig. 5 do not populate the hemispheres equally, C^* and $\tilde{C}$ decrease towards both poles and a north-south symmetry is apparent. The upper and lower bounds of the C-values also drop toward the poles, with the lowest values attained by large ice sheets: Greenland, East Antarctica and West Antarctica have C^* as low as 3.1 $m^{1/2}$, 3.1 $m^{1/2}$ and 2.7 $m^{1/2}$ respectively, whereas the smallest equatorial/mid-latitude value of C^* still exceeds 5 $m^{1/2}$. These trends are opposite to the expectation based on latitudinal control on surface temperature. We postpone their explanation to the end of Section 4.3, and focus first on the bounds in the C-values.

4.3. Dependence of C-values on span

Figs. 7 and 8 plot C^* and $\tilde{C}$ versus L for modern ice masses, showing a large scatter but some clustering in the data. Ice sheets and caps have the lowest (and least variable) C-values whereas valley glaciers have the highest (most variable) C-values; icefields seem intermediate between these groups. As span increases, C^* and $\tilde{C}$ decrease in size and vertical range (variability). These patterns lead to several important results.

First, there are sharp lower bounds in both C-values, with the lowest such bounds (2.7 $m^{1/2}$ for C^*, 2.5 $m^{1/2}$ for $\tilde{C}$) achieved by ice sheets and caps. For valley glaciers such

bounds also exist but take higher values (5.2 $m^{1/2}$ for C^*, 4.1 $m^{1/2}$ for $\tilde{C}$). Because valley glaciers and ice sheets/caps range differently in span, these data reveal an upward transition in each lower bound as L decreases. If we ignore morphological distinction, the bounds may be summarised empirically as curved 'envelopes' given by the equations

$$C^*_{\mathrm{MIN}} = 3.835 - 1.165 \tanh\left(\frac{L - 2\times10^4}{8\times10^3}\right) , \qquad (4)$$

$$\tilde{C}_{\mathrm{MIN}} = 3.4 - \tanh\left(\frac{L - 2\times10^4}{2\times10^4}\right) , \qquad (5)$$

where L is in metres and C^*_{MIN} and $\tilde{C}_{\mathrm{MIN}}$ are the minimum C-values. These approximate envelopes (see Figs. 7 & 8) have been designed with the hyperbolic tangent function to bring out smooth transitions around $L \sim$ 10–50 km.

Second, C^* and $\tilde{C}$ have upper bounds that decay with span, especially for valley glaciers (Figs. 7 and 8a). To explain this, we recognise that while bed topography is not accounted for by the Nye model, it can influence the surface profiles of small ice masses. Notably, for glaciers whose thickness is much less than their bed-elevation range, this range will dominate their relief H so that a steep bed causes high C-values. As the Earth's relief rarely exceeds a few kilometres, H is also limited. These arguments imply a theoretical maximum for C^*: if we suppose the Earth's relief to be at most 2 km (adjustable, order-of-magnitude estimate) and equate it to H, then Eqn. (3) gives $C^*=2000/\sqrt{L}$. It is seen that this envelope mimics the decay in Fig. 7a, attesting the effect of bed topography in our data. In this explanation, ice masses overlying flat basal topography will experience less enhancement in their C-values. It follows that bed-slope differences may also underlie the large variability in C^* and $\tilde{C}$ for small ice masses with similar span.

The situation for the large ice masses is different. Figs. 7 and 8 show that although Antarctica and Greenland contribute only three data points, their C^* do not follow (nor fall below) the theoretical decay $2000/\sqrt{L}$, and their C^* and $\tilde{C}$ occupy a narrow range (2.5–3.3 $m^{1/2}$). For $L >$ tens of km's, there is a striking absence of high values of C. Also, the surface profiles of ice masses at this size are nearly parabolic because the best fits to find their $\tilde{C}$ have high r^2 (>0.8; Fig. 8b), and $C^* \approx \tilde{C}$. These results show that the shape of

large ice masses reflects a pure 'unconstrained spreading' flow that is basically unaffected by bed topography (which makes sense because thick ice drowns basal roughness).

Following these ideas, the observed transitions in the lower bounds of C^* and $\tilde{C}$ can be taken to mean that, for small ice masses, bed topography is able to increase C^* and $\tilde{C}$ above their lowest values (for unconstrained spreading) even when it is as subdued as possible. Such 'residual' effect can be explained because most small glaciers, icefields and ice caps exist in mountain regions, where influence from bed slopes and valley sides is unavoidable. However, to quantify why the effect takes hold as L drops through 10^5 to 10^4 km and raises the C-values by ≈2 (almost doubling them) requires morphometric analysis of mountain landscapes that goes beyond the scope of this paper.

In summary, we think that three key factors govern the C-values of modern ice masses: (i) their 'pure' spreading behaviour (controlled by ice viscosity and basal mechanics, e.g. sliding), which ideally yields C^*, $\tilde{C} \approx 2.5–3.3$ $m^{1/2}$; (ii) their bed topography, whose presence tends to increase C^* and $\tilde{C}$; and (iii) their size (the effect of (ii) becomes stronger as L decreases). The latitudinal plots in Fig. 5 can be understood in terms of these factors. Because 'stiffening' of ice by cold polar temperatures does not cause higher C-values, this effect must be offset by factors (ii) and (iii). In fact, we expect these factors to become more important as we go towards lower latitudes because the ice masses generally reduce in size. The observed patterns in Fig. 5 are consistent with this idea.

5. Glacial reconstruction with *C*-values

Our 'modern' data are now used in the problem of reconstructing palaeo ice masses whose span is known from landform evidence. We focus on the C vs. L relations in Figs. 7 and 8. To reiterate, our central assumption in this paper is that *palaeo ice masses look like modern ones*, and this suggests two uses of the data. An obvious use is to validate reconstructions: the surface shape of palaeo ice masses should have C^* and $\tilde{C}$ falling within the modern data populations, otherwise they fail the analogy and could be viewed as implausible. In Section 5.3 we put published reconstructions to this test.

But first we investigate a forward method which uses the data to guide reconstruction directly (Section 5.1). Although the scatter of C^* and $\tilde{C}$ in Figs. 7 and 8 means that these parameters cannot be reliably estimated from span (except perhaps for the largest ice masses), their upper and lower bounds could be exploited. We reject the upper bounds here for their uncertain dependence on bed slope. However, we use the lower

bounds C^*_{MIN} and $\tilde{C}_{\mathrm{MIN}}$—calculated via Eqns. (4) and (5)—in two steps, each constraining different aspects of the palaeo ice surface, to form what we call a 'minimum reconstruction'. Section 5.2 then applies this method to an area in Kamchatka.

5.1. Forward method

Step 1: Constraining palaeo ice-surface relief

Consider a glaciated mountain terrain in sectional view (Fig. 9). The section is chosen to cross the lowest col in the area of interest and is based on map- or DEM-elevations taken along palaeo ice-flow directions indicated by striations, streamlined bedforms, or (more crudely) valley axes. (Thus the section is not necessary a plane and may project as a curve in plan view.) Moraines dating to the same glaciation have been identified on both sides of the col. All distances in the section are known.

Did the palaeo ice mass submerge the col when its snout reached the moraines? To answer this, consider first the moraine on one side (Fig. 9a), whose horizontal distance from the col in the section is L. After evaluating $C^*_{\mathrm{MIN}}(L)$ with Eqn. (4), we use Eqn. (3) with $C=C^*_{\mathrm{MIN}}$ to construct a parabola extending from the moraine (dashed in Fig. 9a). Because C^* derives from a two-point fit and parameterises relief (Section 3.2), the elevation where the parabola reaches the col (at $x = L$) indicates the lowest ice-surface relief there (H_{MIN}). Thus we calculate

$$H_{\mathrm{MIN}} = C^*_{\mathrm{MIN}}(L)\sqrt{L} \qquad (6)$$

and compare H_{MIN} to the col–moraine height difference (Fig. 9a). We conclude that the col was ice-covered if the profile crosses above the col, but was either ice-free or ice-covered (an indeterminate case) if the profile crosses below the col.

More generally, consideration of moraines from different sides of a col may suggest different results. The highest minimum constraint is then taken, as only one parabola needs to cross above the col to imply its submergence by ice. Fig. 9 illustrates three possibilities for the two-moraine system (indeterminate in 9a, submergence in 9b & 9c). Note that this method of minimum constraints cannot establish for certain that a given col was ice-free. Also, since moraines 'dated to the same age' still suffer dating uncertainty, the method requires a palaeoglaciologist's assumption that they synchron-

ously delimit a glacial event. (This may not matter if the ice masses on different sides were disconnected because the col was ice-free, but we do not know that.)

If the ice mass is large or its bed topography is subdued, so that thick ice may have submerged the col, careful interpretation of geomorphological indicators of ice-flow direction would be necessary to determine the ice-divide position, which may be offset from the col by a long way. In this case, the choice of L for each moraine should be based on the ice divide, not on the col.

Step 2: Constraining the 'minimum surface' and glaciation style

Next we use the (best-fit) shape parameter $\tilde{C}$ to constrain the palaeo ice surface between each moraine and the col. This is important for determining the glaciation style (valley glacier, icefield, or ice cap/sheet), a three-dimensional property that is not strictly inferrable from the last step, although it is true that an ice-free col would suggest separate valley glaciers on different sides and an ice-covered col would rule this out. Knowledge of the three-dimensional palaeo surface also enables the calculation of ELA, where a correctly identified glaciation style is critical (Golledge, 2007).

With L defined as before for each moraine, we evaluate $\tilde{C}_{\mathrm{MIN}}(L)$ from Eqn. (5) and use Eqn. (1) (Nye's model) with $C=\tilde{C}_{\mathrm{MIN}}$, that is,

$$h_{\mathrm{MIN}}(x) = \tilde{C}_{\mathrm{MIN}}(L)\sqrt{x}\,, \qquad (7)$$

to construct the lowest plausible surface trajectory h_{MIN}, where x points up-glacier from the moraine in the section. In three dimensions, this trajectory lies in a (curved) vertical section, and we extend it laterally to form the minimum palaeo ice surface. Specifically, we build such surfaces from different moraines to form a composite minimum surface to see how this intersects the bed topography of the region. If the composite surface lies above much of the bed, we infer an icefield or ice-cap glaciation style; if it lies below the bed to expose many ridges and headwalls as well as nunataks, then the glaciation style remains indeterminate but a valley-glacier morphology cannot be ruled out. This procedure is explained through an example in the next Section. We emphasise our use of Eqn. (7) as a *guide*: While it identifies any reconstructed palaeo surfaces with $\tilde{C} < \tilde{C}_{\mathrm{MIN}}$ to be implausible, it does not imply that the palaeo surface was exactly parabolic in shape.

5.2. Case study in Kamchatka, far-eastern Siberia

The region of interest here (Fig. 10) lies at the southern end of the Sredinny Mountain Range in Kamchatka and is part of our ongoing study of the glacial history of the area (Barr et al., 2007; Barr, 2009; Barr and Clark, 2009). The Kamchatka peninsula has abundant glacial geomorphological evidence. It constitutes the largest glaciated area in northeast Asia today (Solomina and Calkin, 2003) and was glaciated extensively during the Late Quaternary, but the precise extent, timing, and style of glaciation remain uncertain (Bigg et al., 2008 and references therein). Deciphering these variables will help unravel the palaeoclimate of East Siberia and the North Pacific.

Fig. 10 shows our steps of arriving at a minimum glacial reconstruction for the area. We have previously mapped moraines from the SRTM digital elevation data (Barr and Clark, 2009), and Fig. 10a shows two moraines, M_1 and M_2, on the two sides of the range. Shown also are inferred centre ice-flow lines and hydrological catchments upvalley from the moraines. Lacking information on local trimlines, we wish to constrain the palaeo ice cover associated with M_1 and M_2. We do not know the age of these moraines but assume that they relate to the same glacial phase for this reconstruction.

As outlined before, we first use the C^* data of modern glaciers (based on two-point fits through their surface profiles) to constrain the minimum palaeo ice-surface near the col. The results, found with Eqn. (6) in the longitudinal section of each catchment, are marked by two crosses in Fig. 10b. The upper cross indicates that the col must have been submerged by >120 m of ice, which in turn suggests an ice cap or icefield may have covered the higher topography in the area. Valley-glacier style glaciation can be ruled out.

The next step uses the $\tilde{C}$ data of modern glaciers (which best-fits parabolas to their surface profiles) to constrain the continuous ice surface in each catchment. This is done with Eqn. (7), and Fig. 10b shows the resulting minimum parabolas. In this case, the parabola stemming from M_2 predicts an ice-covered col, thereby also ruling out valley glaciers. Fig. 10b shows a complete minimum ice surface formed by joining the parabolas across the divide constraint by hand. When this is projected in three dimensions and extended sideways until it meets the valley walls (straightforward to do in ArcGIS), it produces the ice cover in Fig. 10d. Because this 'ice mass' expresses a minimum constraint, we are not worried that its planform looks unusual (wide main trunk fed by

narrow catchments), and neither have we curved its surface contours deliberately to make them look realistic. The actual palaeo surface is expected to lie above this surface.

We are left to wonder whether the palaeo ice mass was an icefield or ice cap, and for estimating its ELA we need to know its surface topography. We therefore move away from constraints here and consider what our modern dataset tells us to be 'typical'; by this we mean that the ice mass's C-values should land *among* the modern values. We first identify the approximate range of modern C-values at the relevant spans (46.1 km for catchment 1, 21.1 km for catchment 2), as shown by the vertical grey bars in Figs. 7a and 8a, and we choose C^* and $\tilde{C}$ from halfway up each range (a tentative, non-unique choice). Nye parabolas are then constructed in both catchments to find surface profiles and divide elevations, yielding four estimates in total (Fig. 10c). Although these do not agree, pragmatically we draft a surface profile to best accommodate them. Fig. 10e shows the plan view of this reconstruction, which indicates an icefield by the extensive intersections of its surface with sidewalls. This icefield's ELA is 944 m if we apply the Balance-Ratio Method (Furbish and Andrews, 1984; Benn and Gemmell, 1997), assuming a balance ratio of 2. (In this method, which uses the known glacier hypsometry and the assumed ratio between linear mass-balance gradients below and above the equilibrium line, the ELA takes a value that ensures zero overall balance for the glacier.)

In this example, alternative reconstructions could be made by the traditional hand-drawing approach, but without elevation constraints from trimlines this is difficult and uncertain. Our reconstructions, guided by modern data, are more objective. Reconstructions can also be made via the flowline model (Section 2) but require trimline positions again, if not an assumed basal shear stress (Benn and Hulton, 2010). It follows that extensive empirical analysis of the basal shear stress for modern ice masses—as done here for C in Nye's model—will also benefit reconstructions using the flowline model.

5.3. Assessing published reconstructions

In this final analysis, we examine the plausibility of 86 palaeo ice masses from around the world (Table 2) by comparing their shape with modern ones. Published in peer-reviewed literature, these ice masses were chosen mainly for the availability of information regarding their three-dimensional surface, but some of them have considerable palaeo-glaciological significance too. Among their reconstruction approaches are 4 examples of flowline modelling, 1 example of numerical ice-sheet modelling, 1 example

of glacio-isostatic inversion, and 2 examples of the use of theoretical surface profiles; the rest used the hand-drawing approach.

For each ice mass, the method in Section 3 was used to extract surface profiles (typically from map contours) and derive the mean span L and C-values. Fig. 11 plots C^* and $\tilde{C}$ against span for all 86 ice masses, showing also modern data in the background. Reassuringly, 88% of them plot among the modern populations and above the minimum envelopes (C^*_{MIN} and $\tilde{C}_{MIN}$); their profile shape is thus 'plausible' for being indistinguishable from those of the modern ice masses. Below the envelopes, however, plot 10 palaeo ice masses (numbered in Table 2 and Fig. 11). Two of these are reconstructions of the Laurentide Ice Sheet—these are probably acceptable because their data plot only slightly below the envelopes, which are themselves approximate. Of the remaining 8 palaeo ice masses, all from Scotland, two are icefields (including the Drumochter Icefield; see Fig. 1a), three are cirque glaciers, and three are 'saddle glaciers' that spill into opposite valleys from relatively small source areas situated on topographic highs.

What could have caused these outliers? If we assume that the 8 ice masses had their extent reliably constrained by (well-dated, correctly-assembled) moraines, trimlines, and other landforms in the reconstructions, then our analysis shows their surface profiles to be anomalously shallow. One reason for this is *underestimation* of their maximum elevation. In the lack of geomorphic evidence at altitude, which is common, this elevation is difficult to fix, and we think that it is more likely for reconstructionists to suppose thinner ice that exposes some bed topography, than thicker ice that submerges the bed everywhere (the maximum elevation would then be a guess). Such tendency would lower C^* and $\tilde{C}$. In this connection, in McDougall's (2001) reanalysis of the glacial cover in the central Lake District, England during the Loch Lomond Stadial, he pointed out that many palaeo icefields could have been reconstructed incorrectly as cirque and valley glaciers. More generally, the tendency discussed here may mean that many of the palaeo C-values in Fig. 11 may be biased, reduced systematically from the modern data.

5.4. Limitations

Although our preceding results would seem to challenge the credibility of some published reconstructions, we raise important caveats. First, our modern data may not encompass the full range in L–C space, and we welcome efforts to collect more ice masses to resolve the envelopes more accurately. Other morphological measures besides

the *C*-values should also be investigated. Moreover, the possibility should not be overlooked that all of the 86 palaeo ice masses are in fact correct, but fundamental glaciological and climatic differences exist between palaeo and modern ice masses to decouple their *C*-values. If this is true, the use of modern analogues in reconstructions (and so central to this paper) is itself called into question. We leave this outstanding philosophical issue for future research to tackle. For these reasons, it is best to label implausible reconstructions meanwhile as 'unlikely', and certainly not 'wrong'.

Another caveat relates to transient glacier response to changing climate, which could potentially have changed the modern *C*-values in ways that complicate their use in reconstructions. Many modern ice masses worldwide, notably valley glaciers, have experienced thinning and/or frontal retreat under regional warming; it is unknown how much the corresponding adjustments in ice-surface profiles modified C^* and $\tilde{C}$ from their values for steady-state ice masses. Thinning and frontal retreat, respectively, would cause underestimation and overestimation of modern C^* and $\tilde{C}$, while frontal retreat decreases *L* and shifts the modern data in Figs. 7, 8, and 11 towards the left. In a complete (long-term) response, combined thinning and frontal retreat of an ice mass would have effects on the *C*-values that cancel partially, although these processes may differ across ice masses as well as across different stages of the transient response (one process may dominate initially), and we acknowledge that our data collection (Section 3.1) does not quantify these processes. Nevertheless, any resulting numerical bias on C^* and $\tilde{C}$ is expected to be small; even if significant, it does not invalidate our proposed reconstruction tools because numerical ice-flow models of the transient evolution can (in principle) be used to correct bias due to the establishment of characteristic profiles during glacier advance and retreat. We also note that the caveat raised here applies generally to other reconstruction approaches. Practitioners who use the hand-drawing method or flowline model rarely recognise the dynamism of modern ice masses when deriving data for their analogue (of shape or basal shear stress), or recognise explicitly whether their reconstructed ice masses are equilibrium forms. These considerations should stimulate further work that refines the use of analogues in palaeo-glacier reconstructions.

6. Conclusions

In this paper, we have analysed the shape of modern ice masses, focusing on the relationships between their horizontal scale (span, *L*) and two parameters, C^* and $\tilde{C}$, that

characterise the relief and steepness of their surface profiles. The *C*-values derive from using Nye's plastic ice-sheet model as a parameterisation. Our data yield insights on the morphology and flow of ice masses globally (Section 4). As their size increases, their profiles become more parabolic because the effect of bed topography becomes dominated by an 'unconstrained spreading' tendency of ice flow. Thus, C^* and $\tilde{C}$ of the largest ice masses tend towards 2.5–3.3 $m^{1/2}$, but, for smaller ice masses, are higher and more variable (Figs. 7 and 8). Although the competing influences of flow and basal roughness on glacier morphology may seem obvious, our dataset quantifies this competition and its scale-dependence for the first time.

Importantly, the discovery of minimum bounds in C^* and $\tilde{C}$ (Eqns. (4) and (5)) led us to develop practical methods for constraining glacier reconstructions (Section 5). Given past glacial limits, these bounds allow us to estimate the lowest palaeo ice surface consistent with the modern variety of surface profiles, and this also constrains the corresponding palaeo glaciation style and ELA. Used in a different way, the bounds can adjudicate the plausibility of reconstructions. While minimum constraints may seem less powerful than absolute ones, we emphasise that glacier reconstructions have inherent uncertainties, so it is as important to recognise these as to strive towards unique results. In our Kamchatkan case study, for instance, the 'typical' reconstruction (Fig. 10e) would change markedly had we chosen different values of C^* and $\tilde{C}$, but the range of these parameters in Figs. 7 and 8 informs us reliably of the range of acceptable reconstructions. Viewed in this light, directional (maximum/minimum) constraints can be very valuable, and we advocate searching for more of them. The design of new tools using them to reduce the subjectivity of reconstructions has considerable potential, and could also involve more glacier physics than has been used in the current study.

Morphometric analyses are common in many areas of geomorphology for enabling (i) rigorous descriptions of forms and (ii) tests of physical understanding against observations. While not new in glaciology, they should be explored further. Hitherto, size-volume scalings have been used to predict the sea-level impact of glaciers (Bahr et al, 1997), and ELA estimation has long relied on glacier area properties (see Benn et al., 2005). This paper has pursued the same spirit. Besides properties of surface profiles along flow lines, many other attributes of the complex shape of ice masses may be investigated (e.g. three-dimensional surface curvature, the topology of glacier networks). Studying

them is now timely, given a recent explosion in the availability of new datasets that can resolve the Earth's surface elevation at unprecedented resolution and accuracy.

Acknowledgments

We thank Arjen Stroeven and an anonymous reviewer for careful and helpful comments that improved this manuscript, and specifically, the latter reviewer for pointing out that warming-induced glacier recession may bias modern *C*-values, which led us to add the last paragraph in Section 5.4.

References

Allen, R., Siegert, M.J., Payne, A.J., 2008. Reconstructing glacier-based climates of LGM Europe and Russia — Part I: numerical modelling and validation methods. Climate of the Past 4, 235–248.

Andrews, J.T., 1982. On the reconstruction of Pleistocene ice sheets: a review. Quaternary Science Reviews 1, 1-30.

Bahr, D.B., Meier, M.F., Peckham, S.D., 1997, The physical basis of glacier volume-area scaling. Journal of Geophysical Research 102(B9), 20355-20362.

Balascio, N.L., Kaufman, D.S., Manley, W.F., 2005. Equilibrium-line altitudes during the Last Glacial Maximum across the Brooks Range, Alaska. Journal of Quaternary Science 20, 821-838.

Ballantyne, C.K., 1989. The Loch Lomond Readvance on the Isle of Skye, Scotland: glacier reconstruction and palaeoclimatic implications. Journal of Quaternary Science 4(2), 95-108.

Ballantyne, C.K., 2002. The Loch Lomond Readvance on the Isle of Mull, Scotland: glacier reconstruction and palaeoclimatic implications. Journal of Quaternary Science 17(8), 759-771.

Ballantyne, C.K., 2007a. Loch Lomond Stadial glaciers in North Harris, Outer Hebrides, North-West Scotland: glacier reconstruction and palaeoclimatic implications. Quaternary Science Reviews 26, 3134-3149.

Ballantyne, C.K., 2007b. The Loch Lomond Readvance on north Arran, Scotland: glacier reconstruction and palaeoclimatic implications. Journal of Quaternary Science 22(4), 343-359.

Ballantyne, C.K., Wain-Hobson, T., 1980. The Loch Lomond Advance on the Island of Rhum. Scottish Journal of Geology 16(1), 1-10.

Ballantyne, C.K., Stone, J.O., McCarroll, D., 2008. Dimensions and chronology of the last ice sheet in Western Ireland. Quaternary Science Reviews 27, 185-200.

Barr, I.D., 2009. Constraining the extent, style and phases of glaciation to derive Late Quaternary equilibrium-line altitude estimates in Far NE Russia. Ph.D Thesis, University of Sheffield, UK.

Barr, I.D., Clark, C.D., 2009. Distribution and pattern of moraines in Far NE Russia reveal former glacial extent. Journal of Maps, 186-193.

Barr, I.D., Clark, C., Ng, F., 2007. Constraining the Late-Quaternary glaciation extent in Kamchatka by combining geomorphology and an empirical shape-characterisation for modern ice masses (Abstract). The XVII INQUA Congress, Cairns, Australia, August 2007.

Benn, D.I., Ballantyne, C.K., 2005. Palaeoclimatic reconstructions from Loch Lomond Readvance glaciers in the West Drumochter Hills, Scotland. Journal of Quaternary Science 20(6), 577-592.

Benn, D.I., Gemmell, A.M.D., 1997. Calculating equilibrium-line altitudes of former glaciers by the balance ratio method: a new computer spreadsheet. Glacial Geology and Geomorphology (http://ggg.qub.ac.uk/papers/full/1997/tn011997/tn01.html).

Benn, D.I., Hulton, N.R.J., 2010. An Excel™ spreadsheet program for reconstructing the surface profile of former mountain glaciers and ice caps. Computers and Geosciences 36(5), 605-610.

Benn, D. I., Owen, L. A., Osmaston, H. A., Seltzer, G. O., Porter, S., Mark, B., 2005. Reconstructing equilibrium-line altitudes for tropical and sub-tropical glaciers. Quaternary International 138-139**,** 8-21.

Bigg, G.R., Clark, C.D., Hughes, A.L.C., 2008. A last glacial ice sheet on the Pacific Russian coast and catastrophic change arising from coupled ice-volcanic interaction. Earth and Planetary Science Letters 265, 559–570.

Boulton, G., Hagdorn, M., 2006. Glaciology of the British Isles Ice Sheet during the last glacial cycle: form, flow, streams and lobes. Quaternary Science Reviews 25, 3359-3390.

Brugger, K.A., 2006. Late Pleistocene climate inferred from the reconstruction of the Taylor River glacier complex, southern Sawatch Range, Colorado. Geomorphology 75, 318-329.

Clark, P.U., Mix, A.C., 2000. Ice sheets by volume. Nature 406, 689-690.

CLIMAP Project Members, 1981, Seasonal reconstruction of the Earth's surface at the last glacial maximum. Geological Society of America, Map and Chart Series, MC-36-1981.

Dyke, A.S., Andrews, J.T., Clark, P.U., England, J.H., Miller, G.H., Shaw, J., Veillette, J.J., 2002. The Laurentide and Innuitian ice sheets during the Last Glacial Maximum. Quaternary Science Reviews 21(1), 9-31.

Fowler, A.C., 1992. Modelling ice sheet dynamics. Geophysical and Astrophysical Fluid Dynamics 63, 29–65.

Fredin, O., 2004. Mountain centered icefields in Northern Scandinavia. Comprehensive summary of Ph.D thesis, Stockholm University, Sweden. (Download fulltext from http://su.diva-portal.org/smash/record.jsf?pid=diva2:189838)

Furbish, D.J., Andrews, J.T., 1984. The use of hypsometry to indicate long-term stability and response of valley glaciers to changes in mass transfer. Journal of Glaciology 30(105), 199-211.

Golledge, N.R., 2007. An ice cap landsystem for palaeoglaciological reconstructions: characterizing the Younger Dryas in western Scotland. Quaternary Science Reviews 26**,** 213-229.

Golledge, N.R., Hubbard, A., 2005. Evaluating Younger Dryas glacier reconstructions in part of the western Scottish Highlands: a combined empirical and theoretical approach. Boreas 34**,** 274-286.

Golledge, N.R., Hubbard, A., Sugden, D.E., 2008. High-resolution numerical simulation of Younger Dryas glaciation in Scotland. Quaternary Science Reviews 27, 888-904.

Hubbard, A., Sugden, D., Dugmore, A., Norddahl, H., Pétursson, H.G., 2006. A modeling insight into the Icelandic Last Glacial Maximum ice sheet. Quaternary Science Reviews 25(17-18), 2283-2296.

Hughes, T.J., 1981. Numerical reconstruction of palaeo-ice sheets. In: Denton, G.H., Hughes, T.J. (Eds.), The Last Great Ice Sheets. Wiley, New York, pp. 221–261.

Hutter, K., 1983. Theoretical Glaciology. Reidel, Dordrecht, The Netherlands.

Kaser, G., Osmaston, H.A., 2002. Tropical Glaciers. Cambridge University Press, Cambridge.

Kleman, J., Borgström, I., 1996. Reconstruction of palaeo-ice sheets: the use of geomorphological data. Earth Surface Processes and Landforms 21, 893-909.

Lachniet, M.S., Vazquez-Selem, L., 2005. Last Glacial Maximum equilibrium line altitudes in the circum-Caribbean (Mexico, Guatemala, Costa Rica, Columbia, and Venezuela). Quaternary International 138-139, 129-144.

Locke, W.W., 1995. Modelling of icecap glaciation of the northern Rocky Mountains of Montana. Geomorphology 14, 123-130.

Mark, B.G., Harrison, S.P., Spessa, A., New, M., Evans, D.J.A., Helmens, K.F., 2005. Tropical sowline changes at the last glacial maximum: A global assessment. Quaternary International 138-139, 168-201.

McDougall, D.A., 2001. The geomorphological impact of Loch Lomond (Younger Dryas) Stadial plateau icefields in the central Lake District, northwest England. Journal of Quaternary Science 16, 531–543.

Meier, M.F., Post, A.S., 1962. Recent variations in mass net budgets of glaciers in western North America. International Association of Scientific Hydrology 58, 63-77.

Meierding, T.C., 1982. Late Pleistocene glacial equilibrium-line altitudes in the Colorado Front Range: a comparison of methods. Quaternary Research 18**,** 289-310.

National Snow and Ice Data Center, 1999, updated 2009. *World Glacier Inventory*. World Glacier Monitoring Service and National Snow and Ice Data Center/World Data Center for Glaciology. Boulder, CO. Digital media.

Nye, J.F., 1951. The flow of glaciers and ice-sheets as a problem in plasticity. Proceedings of the Royal Society of London, Series A, Mathematical and Physical Sciences 207, 554–572.

Nye, J.F., 1952. A method of calculating the thicknesses of the ice sheets. Nature 169, 529–530.

Osmaston, H., 2005. Estimates of glacier equilibrium line altitudes by the Area × Altitude, the Area × Altitude Balance Ratio and the Area × Altitude Balance Index methods and their validation. Quaternary International 138-139**,** 22-31.

Paterson, W.S.B., 1994. The Physics of Glaciers. 3rd ed. Pergamon, Oxford.

Peltier, W.R., 2004. Global glacial isostasy and the surface of the Ice-Age Earth: the ICE-5G (VM2) Model and GRACE. Annual Review of Earth and Planetary Sciences 32, 111-149.

Porter, S.C., 2001. Snowline depression in the tropics during the Last Glaciation. Quaternary Science Reviews 20**,** 1067-1091.

Rea, B.R., Evans, D.J.A. 2007. Quantifying climate and glacier mass balance in north Norway during the Younger Dryas. Palaeogeography, Palaeoclimatology, Palaeoecology 246, 307-330.

Reeh, N., 1982. A plasticity theory approach to the steady-state shape of a three-dimensional ice sheet. Journal of Glaciology 28, 431–455.

Schilling, D.H., Hollin, J.T., 1981. Numerical reconstructions of valley glaciers and small ice caps. In: Denton, G.H., Hughes, T.J. (Eds.), The Last Great Ice Sheets. Wiley, New York, pp. 207–220.

Sissons, J.B. 1980. The Loch Lomond Advance in the Lake District, northern England. Transactions of the Royal Society of Edinburgh: Earth Sciences 71, 13–27.

Sissons, J.B., Sutherland, D.G., 1976. Climatic inferences from former glaciers in the south-east Grampian Highlands, Scotland. Journal of Glaciology 17, 325-346.

Solomina, O., Calkin, P.E., 2003. Lichenometry as applied to moraines in Alaska, USA, and Kamchatka, Russia. Arctic, Antarctic, and Alpine Research 35, 129–143.

Stansell, N.D., Polissar, P.J., Abbott, M.B., 2007. Last glacial maximum equilibrium-line altitude and paleo-temperature reconstructions for the Cordillera de Mérida, Venezuelan Andes. Quaternary Research 67, 115-127.

Sugden, D.E., 1977. Reconstruction of the morphology, dynamics, and thermal characteristics of the Laurentide Ice Sheet at its maximum. Arctic and Alpine Research 9, 21–47.

Sugden, D.E., John, B.S., 1976. Glaciers and landscape, a geomorphological approach. John Wiley and Sons, New York.

Sutherland, D.G., 1984. Modern glacier characteristics as a basis for inferring former climates with particular reference to the Loch Lomond Stadial. Quaternary Science Reviews 3, 291-309.

Van der Veen, C.J., 1999. Fundamentals of Glacier Dynamics. Balkema, Rotterdam.

Vieira, G., 2008. Combined numerical and geomorphological reconstruction of the Serra da Estrela plateau icefield, Portugal. Geomorphology 97, 190-207.

Winsborrow, M.C.M., 2007. Exploring controls on the location of Laurentide palaeo-ice streams. Ph.D thesis, University of Sheffield, UK.

Captions of Figures and Tables

Figure 1

Examples of glacial reconstructions from the literature. (a) A map of the Loch-Lomond Stade icefield in the West Drumochter Hills, Scotland, reconstructed from geomorphological mapping by the 'hand-drawing' approach (figure redrawn from Fig. 9 of the paper by Benn and Ballantyne (2005)). Dashed lines on the icefield locate surface profiles that have been used to derive the shape parameters in entry no. 4 in Table 2. (b) A numerically-computed surface topography of the British-Irish Ice Sheet at 17 ka (reproduced from Fig. 14 of the paper by Boulton and Hagdorn (2006)).

*** We seek permission with *Quaternary Science Reviews* to reproduce panel (b) while this paper is under review. ***

Figure 2

Mathematical symbols and definitions used in this paper. (a) Nye's (1951, 1952) theoretical parabola, as given by Equation (1). (b) Two ways of fitting the parabola to a sampled ice-surface profile (with sample points shown by dots). A two-point fit (upper dashed line) yields the shape parameter C^*; a best fit (lower dashed line) yields the shape parameters $\tilde{C}$. Note that x is distance up-glacier along a flowline (which usually describes a curve in plan view).

Figure 3

Location of the 200 modern ice masses from which surface profiles were extracted for the analysis of this paper. See Table 1 for the morphological data of these ice masses.

Figure 4

(a) Relief H against span L for the modern ice masses of our dataset. (b) Enlargement of panel (a) for $0 \leq L \leq 60$ km. This range excludes the three data points shown in (a) for East Antarctica and West Antarctica and Greenland. In both panels, symbols identify different types of ice masses.

Figure 5

Latitudinal distribution of (a) the shape parameter C^* (deriving from two-point fits of surface profiles) and (b) the shape parameter $\tilde{C}$ (deriving from best fits of surface profiles) for the modern ice masses of our dataset.

Figure 6

Relation between the shape parameters $\tilde{C}$ and C^* for the modern ice masses of our dataset. Most data points fall under the dashed line, in the region $C^* > \tilde{C}$.

Figure 7

(a) The (two-point fit) shape parameter C^* plotted against span L for the 200 modern ice masses of our dataset. L is in logarithmic scale. The cluster of three data points at the lower right of the plot derive from the Antarctic and Greenland Ice Sheets. The solid line and dashed line, respectively, are the lower and upper envelopes discussed in Section 4.3. Vertical grey bars show the approximate ranges of C^* used later in the reconstruction of Fig. 10. (b) Enlargement of panel (a) for $0 \leq L \leq 60$ km (linear scale). Data for ice sheets and ice caps have been ignored.

Figure 8

(a) The (best-fit) shape parameter $\tilde{C}$ against span L for the 200 modern ice masses of our dataset. L is in logarithmic scale. The cluster of three data points at the lower right of the plot derive from the Antarctic and Greenland Ice Sheets. The solid line is the approximate lower envelope of the data $\tilde{C}_{\mathrm{MIN}}(L)$, discussed in Section 4.3. Vertical grey bars show the approximate ranges of $\tilde{C}$ used later in the reconstruction of Fig. 10. (b) Average r^2-values of the best fits for the surface profiles of each ice mass that yield the corresponding shape parameter $\tilde{C}$ in (a).

Figure 9

Minimum constraints in glacier reconstruction for a mountain topography. Given moraine position M and its horizontal distance from the col, L, the equation $H_{MIN} = C^*_{MIN}\sqrt{L}$ (with C^*_{MIN} given by Eqn. (4)) is used to find the minimum palaeo ice-surface elevation at the col (H_{MIN} uses the moraine elevation as datum). A cross marks the minimum elevation thus inferred from each moraine. Crosses associated with different moraines (M_1 and M_2) are used to judge whether the ice mass submerged the col. For the three scenarios, we conclude that (a) yields an indeterminate result whereas ice submerged the col in (b) and (c). Note that the sectional view is made along palaeo flowlines or valley axes, thus it is not necessary planar and may project as a curve in plan view.

Figure 10

Glacial reconstruction with C-values, applied to an area of the Sredinny Mountains in Kamchatka near 54˚N, 157˚E. (a) Mapped moraine positions M_1 and M_2, catchment boundaries (solid), and valley axes (dashed) overlaid on shaded SRTM digital elevations. Inset shows study-area location in Kamchatka. (b) A minimum reconstruction of the palaeo ice-divide elevation (crosses) and palaeo ice surface (parabolas) in a sectional view containing the valley axes. The method of Section 5.1 is used. In each catchment, the moraine elevation serves as datum for the minimum divide relief (H_{MIN}) and minimum surface relief (h_{MIN}). We calculate these by using Eqns. (6) and (7) with L = 46.1 km, $C^*_{MIN} = 2.67$, $\tilde{C}_{MIN} = 2.54$ for catchment 1, and L = 21.1 km, $C^*_{MIN} = 3.67$, $\tilde{C}_{MIN}$ = 3.34 for catchment 2. Dashed line has been added by hand to complete the minimum ice surface. (c) A 'typical' reconstruction of the palaeo ice-divide elevation (crosses) and ice surface (parabolas) in the sectional view. The equations $H_{TYP} = C^*\sqrt{L}$ and $h_{TYP} = \tilde{C}\sqrt{x}$ are evaluated with L = 46.1 km, $C^* = 5.1$, $\tilde{C} = 4.5$ for catchment 1, and L = 21.1 km, $C^* = 7.2$, $\tilde{C} = 6.5$ for catchment 2. Dashed line has been added by hand to complete the typical ice surface. (d) Plan view of the minimum ice cover (white) computed by laterally extending the h_{MIN}-parabolas in (b). (e) Plan view of the typical ice cover (white) computed by laterally extending the h_{TYP}-parabolas in (c). This result indicates an icefield glaciation style.

Figure 11

Comparison of the surface-profile parameters of 86 palaeo ice masses from the literature (listed in Table 2) with those of modern ice masses. (a) A plot of the shape parameter C^* against span L. (b) A plot of the shape parameter $\tilde{C}$ against span L. In both panels, solid dots locate palaeo ice mass data, grey symbols locate the data of 200 modern ice masses from Figs. 7 and 8, and the data points numbered 1 to 10 identify palaeo ice masses whose C^* falls below the minimum envelope $C^*_{MIN}(L)$ in Eqn. (4). The same numbering system is used in Table 2.

Table 1

Geographical coordinates and morphological data of 200 modern ice masses whose surface profiles were analysed in this paper. Columns 6 and 7 show the *mean* span (L) and relief (H) of multiple profiles extracted from each ice mass.

Table 2

Palaeo ice masses in published reconstructions, and parameters L, C^* and $\tilde{C}$ for their surface profiles. Entries are ordered by decreasing span (L). Shaded entries have $\tilde{C} < \tilde{C}_{MIN}$. Methods in column four are: 1 = Hand drawing (observing geomorphic constraints and using modern ice masses as analogues), 2 = iterative flowline modelling, 3 = glacio-isotatic numerical inversion, 4 = three-dimensional thermo-mechanically coupled numerical ice sheet model, 5 = parabolic profiling.

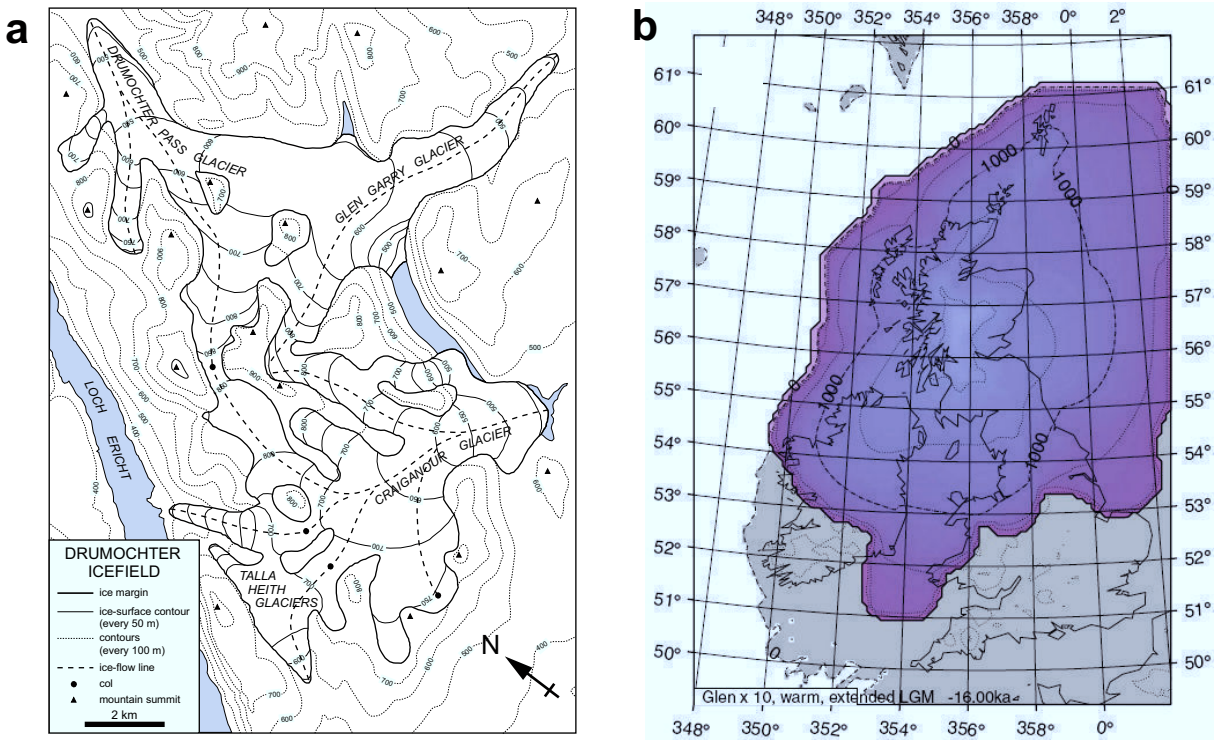

Figure 1 (Ng *et al.*, submitted)

correctly-sized; approx. 160 mm wide;
please position across two columns

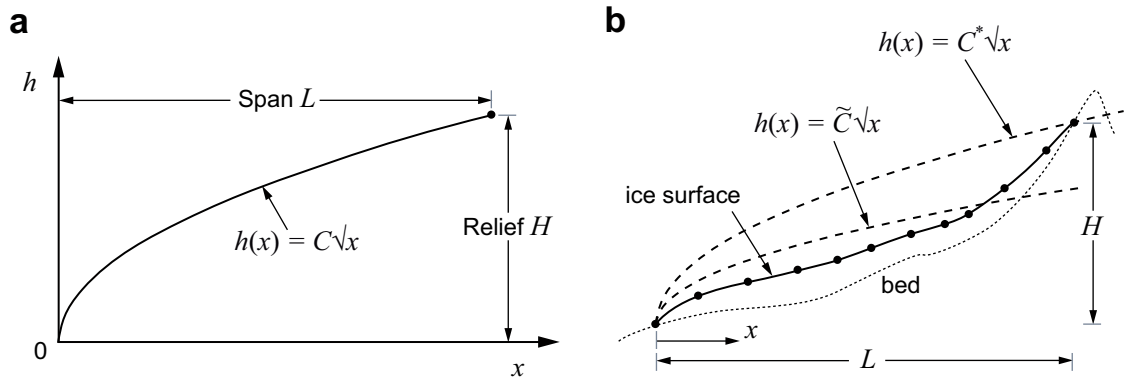

Figure 2 (Ng *et al.*, submitted)

correctly-sized; approx. 150 mm wide;
please position across two-columns

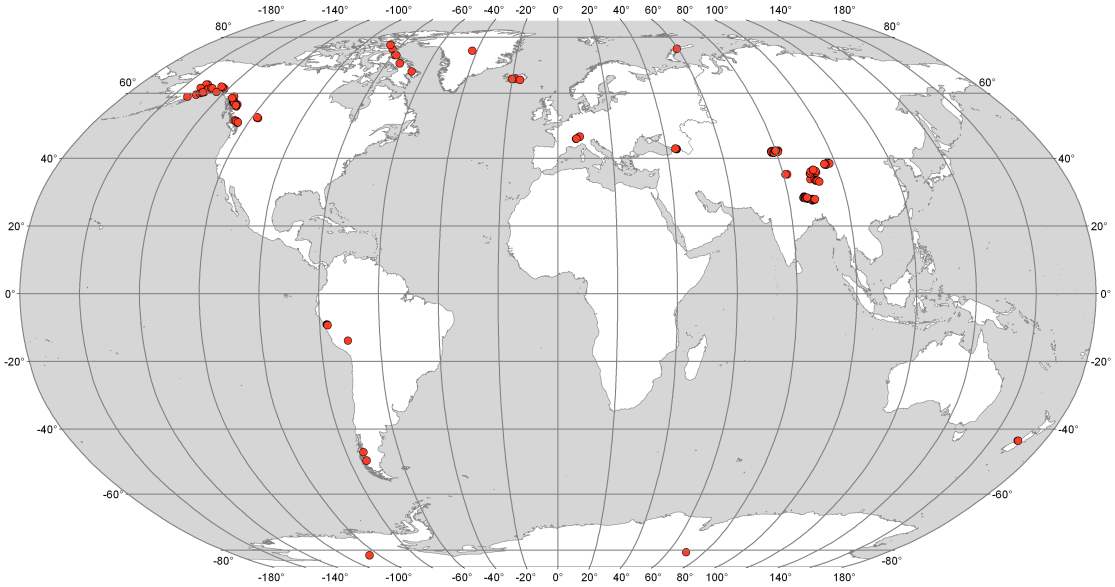

Figure 3 (Ng *et al.*, submitted)

sized-correctly; approx. 150 mm wide;
please position across two columns

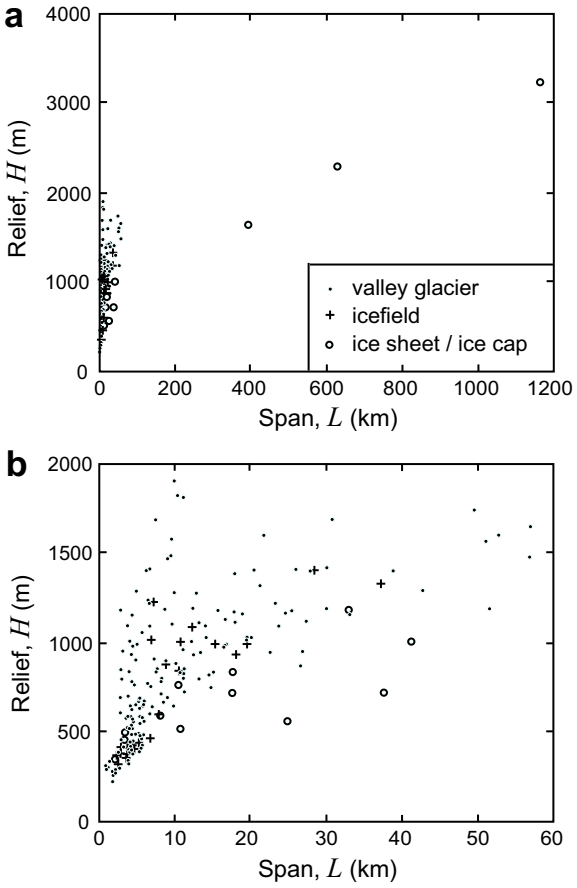

Figure 4 (Ng *et al.*, submitted)

sized-correctly; approx. 76 mm wide;
please position down a column

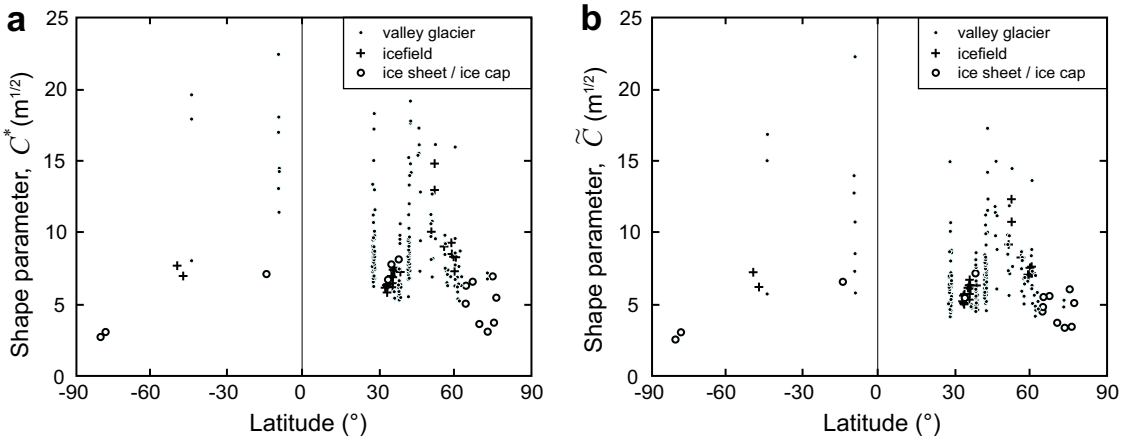

Figure 5 (Ng *et al.*, submitted)

sized-correctly; approx. 150 mm wide;
please position across two columns

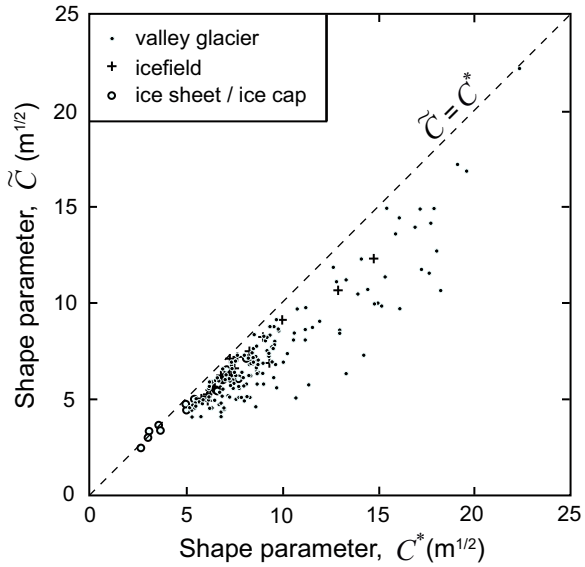

Figure 6 (Ng *et al.*, submitted)

sized-correctly; approx. 76 mm wide;
please position down 1 column

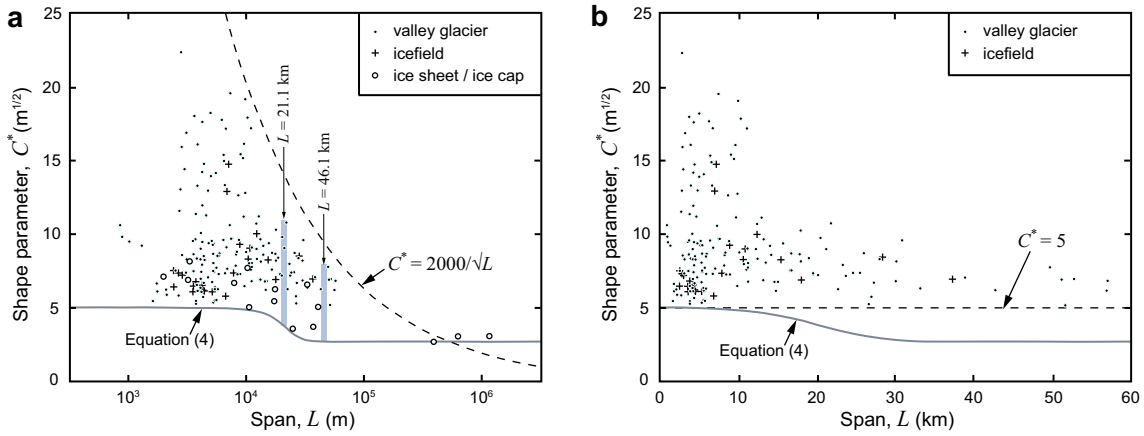

Figure 7 (Ng *et al.*, submitted)

sized-correctly; approx. 150 mm wide;
please position across two columns

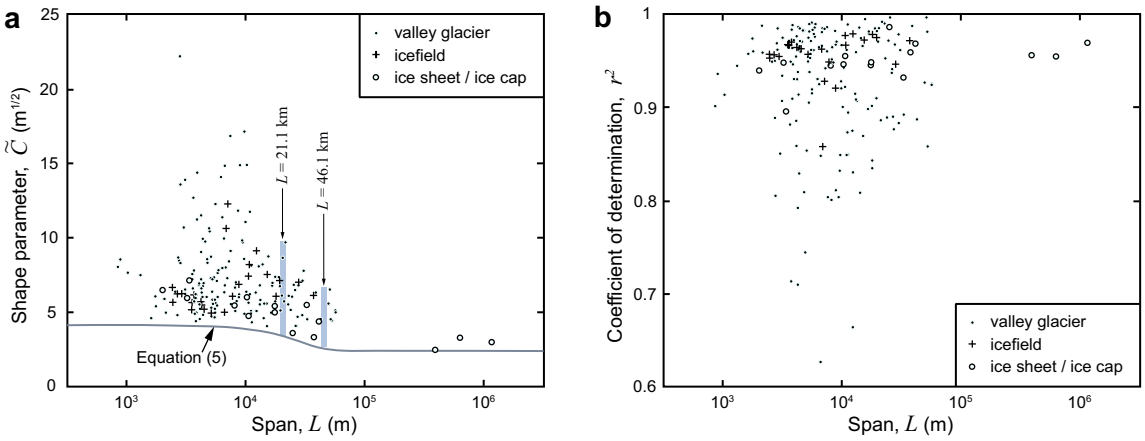

Figure 8 (Ng *et al.*, submitted)

correctly-sized; approx. 150 mm wide;
please position across two columns

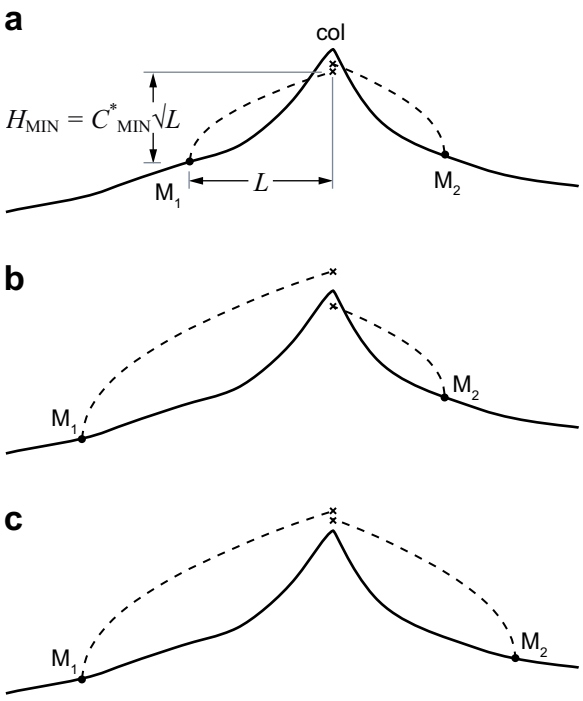

Figure 9 (Ng *et al.*, submitted)

sized-correctly; approx. 76 mm wide;
please position down a column

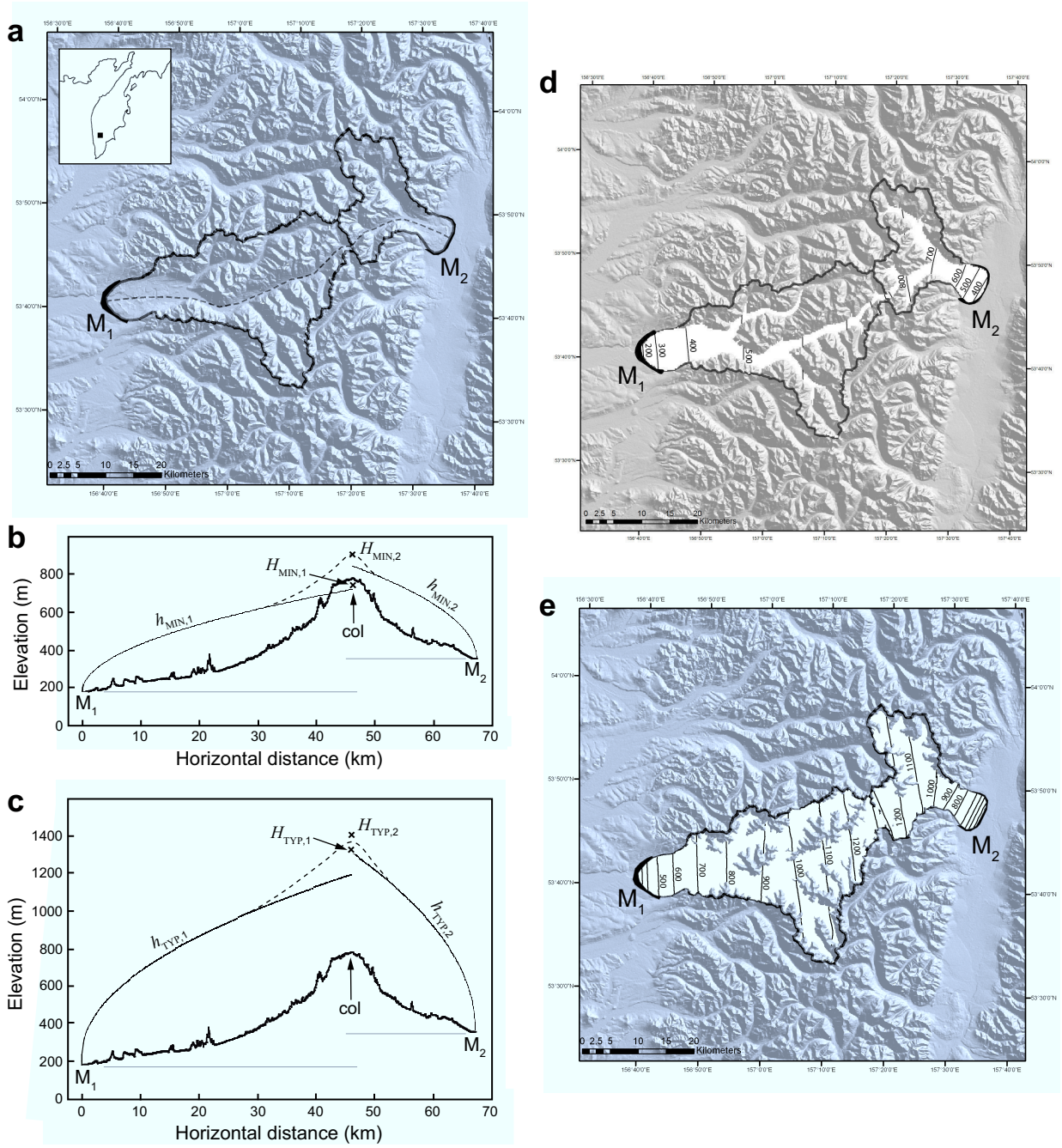

Figure 10 (Ng *et al.*, submitted)

correctly-sized; approx. 164 mm wide;
please position across two columns

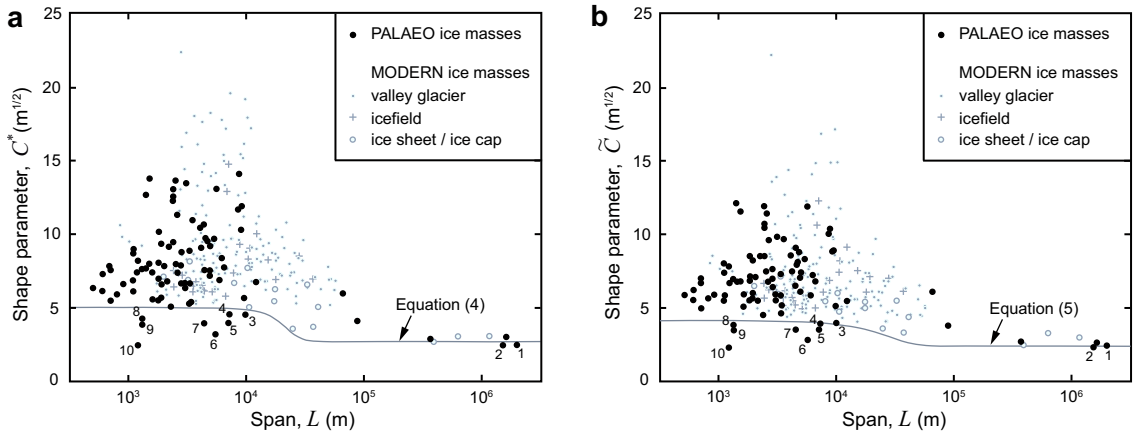

Figure 11 (Ng *et al.*, submitted)

sized-correctly; approx. 150 mm wide;
please position across two columns

Table 1. Geographical coordinates and morphological data of 200 modern ice masses whose surface profiles were analysed in this paper. Columns 6 and 7 show the *mean* span (*L*) and relief (*H*) of multiple profiles extracted from each ice mass.

Geographical region	Name of ice mass (if known)	Morphological type	Latitude	Longitude	Span, *L* (km)	Relief, *H* (m)	C^* ($m^{1/2}$)	$\bar{C}$ ($m^{1/2}$)
Antarctica	East Antarctic Ice Sheet	Ice Sheet	see Fig. 3	see Fig. 3	1164	3234	3.1	3.0
	West Antarctic Ice Sheet	Ice Sheet	see Fig. 3	see Fig. 3	393	1636	2.7	2.5
Greenland	Greenland Ice Sheet	Ice Sheet	see Fig. 3	see Fig. 3	629	2296	3.1	3.3
South America	Quelccaya Ice Cap	Ice cap	-13.92	-70.81	2.0	345	7.2	6.5
	North Patagonia Icefield	Icefield	-46.86	-73.52	37.2	1326	7.0	6.1
	South Patagonia Icefield	Icefield	-48.93	-73.46	36.2	1348	7.7	7.2
	—	Valley Glacier	-9.11	-77.57	4.3	930	14.3	7.3
	Kinzl Glacier (Chopicalqui)	Valley Glacier	-9.07	-77.59	3.8	701	11.4	5.8
	—	Valley Glacier	-9.35	-77.38	3.7	1096	18.1	12.7
	—	Valley Glacier	-9.36	-77.34	3.2	952	16.9	13.9
	—	Valley Glacier	-9.09	-77.55	3.0	796	14.5	10.7
	—	Valley Glacier	-9.23	-77.50	2.8	1182	22.4	22.2
	—	Valley Glacier	-9.18	-77.51	2.8	695	13.0	8.5
New Zealand	Murchison Glacier	Valley Glacier	-43.53	170.28	10.7	832	8.0	5.7
	Fox Glacier	Valley Glacier	-43.51	170.11	10.3	1821	17.9	14.9
	Franz Josef Glacier	Valley Glacier	-43.46	170.18	7.4	1686	19.6	16.9
Iceland	Vatnajökull	Ice Cap	64.42	-16.68	41.1	1004	5.0	4.4
	Hofsjökull	Ice Cap	64.80	-18.82	17.7	839	6.3	5.5
	Langjökull	Ice Cap	64.64	-20.15	10.6	518	5.0	4.8
Russian Arctic	Novaya Zemlya	Ice Cap	75.81	61.97	37.6	720	3.7	3.4
Canadian Arctic	Penny Ice Cap, Baffin Island	Ice Cap	67.25	-66.06	33.0	1184	6.6	5.5
	Barnes Ice Cap, Baffin Island	Ice Cap	70.04	-73.62	24.9	562	3.6	3.6
	Sydkap Ice Cap, Ellesmere Island	Ice Cap	76.87	-85.68	17.6	721	5.5	5.0
	Devon Ice Cap, Devon Island	Ice Cap	75.16	-82.26	3.2	462	6.9	6.0
	Aktineq Glacier, Bylot Island	Valley Glacier	72.95	-78.79	27.2	1121	6.7	4.7
	Sermilik Glacier, Bylot Island	Valley Glacier	72.95	-78.14	23.7	1091	7.2	5.2
Alaska	Juneau Icefield	Icefield	59.01	-134.41	28.3	1404	8.5	7.0
	Harding icefield	Icefield	60.00	-150.01	19.5	991	7.3	7.1
	Sargent icefield	Icefield	60.29	-148.60	15.4	996	8.3	7.5
	Grewingk-Yalik Glacier Complex	Icefield	59.54	-150.85	10.6	844	8.3	7.5
	Mt. Douglas-Fourpeaked Glacier Complex	Icefield	58.83	-153.60	8.9	881	9.3	6.9
	Kahiltna Glacer	Valley Glacier	62.79	-151.29	57.0	1648	6.9	5.1
	Steller Glacier	Valley Glacier	60.39	-143.63	56.9	1482	6.2	5.0
	Nabesna Glacier	Valley Glacier	61.96	-143.04	51.5	1187	5.2	4.6
	Ruth Glacier	Valley Glacier	62.75	-150.62	42.7	1296	6.3	4.6
	Harvard Glacier	Valley Glacier	61.63	-147.57	33.1	1159	6.4	4.6
	—	Valley Glacier	61.36	-148.33	30.0	1192	6.9	4.8
	—	Valley Glacier	61.57	-141.90	26.9	954	5.8	4.1
	—	Valley Glacier	61.60	-146.89	26.6	870	5.3	4.1
	Copper Glacier	Valley Glacier	62.12	-143.75	17.8	1171	8.7	5.8
	Trimble Glacier	Valley Glacier	61.70	-152.13	16.8	985	7.6	7.0

	—	Valley Glacier	61.20	-148.44	14.8	752	6.2	5.6
	—	Valley Glacier	60.12	-149.24	7.0	646	7.7	7.3
	—	Valley Glacier	60.26	-149.14	5.2	689	9.6	8.8
	—	Valley Glacier	60.18	-149.27	4.4	447	6.7	6.1
	—	Valley Glacier	60.18	-149.13	3.8	520	8.4	6.3
	—	Valley Glacier	60.30	-149.04	2.9	853	15.9	13.6
	—	Valley Glacier	60.18	-149.20	2.9	459	8.6	8.4
Alaska (South)	Mendenhall Glacier	Valley Glacier	58.49	-134.54	51.1	1570	6.9	6.6
	Baird Glacier	Valley Glacier	57.14	-132.67	38.8	1399	7.1	6.3
	Dawes Glacier	Valley Glacier	57.48	-132.73	25.5	1178	7.4	6.9
	Mud Glacier	Outlet Glacier	57.01	-131.91	9.8	643	6.5	4.9
Canada Coast Mountains (North)	Cambria Icefield	Icefield	55.88	-129.68	10.8	1004	9.1	8.2
	Flood Glacier	Valley Glacier	57.16	-132.06	22.7	949	6.3	5.5
	Salmon Glacier	Valley Glacier	56.16	-130.07	20.4	1406	9.8	8.6
	Great Glacier	Valley Glacier	56.85	-131.89	19.5	1029	7.4	6.8
	Frank Mackie Glacier	Valley Glacier	56.32	-130.15	18.9	1160	8.4	7.4
	Knipple Glacier	Valley Glacier	56.42	-130.00	14.0	1095	9.2	8.2
	Berendon Glacier	Valley Glacier	56.24	-130.10	6.8	753	9.1	8.0
	Leduc Glacier	Valley Glacier	56.20	-130.33	5.3	550	7.5	5.9
Canada Coast Mountains (South)	Homathko Icefield	Icefield	51.08	-124.56	12.4	1086	10.0	9.1
	Silverthrone Glacier	Valley Glacier	51.43	-125.83	30.1	1421	8.2	7.1
	Breccia Glacier	Valley Glacier	51.28	-125.34	21.8	1594	10.8	9.7
	Smoking Canyon Glacier	Valley Glacier	51.33	-125.06	13.2	797	6.9	5.6
	Bert Glacier	Valley Glacier	51.24	-125.11	8.7	1182	12.7	11.8
	Gilbert Glacier	Valley Glacier	50.84	-124.09	7.5	843	9.7	9.1
	Falcon Glacier	Valley Glacier	50.83	-124.19	7.3	910	10.6	8.5
	Esdras Glacier	Valley Glacier	50.87	-124.20	5.3	587	8.1	7.3
	Eridanus Glacier	Valley Glacier	50.85	-124.02	4.6	763	11.3	9.8
Canadian Rockies	Clemenceau Icefield	Icefield	52.19	-117.82	7.2	1233	14.8	12.3
	Columbia Icefield	Icefield	52.14	-117.30	6.9	1016	13.0	10.7
	—	Valley Glacier	52.42	-118.00	3.9	1011	16.1	14.4
	—	Valley Glacier	52.44	-118.02	3.6	576	9.5	7.6
Alps	Aletschgletscher	Valley Glacier	46.47	8.06	15.7	1178	9.4	8.8
	Glacier du Tacul (Mer de Glace)	Valley Glacier	45.88	6.93	11.0	1812	17.3	11.8
	Fieschergletscher	Valley Glacier	46.50	8.14	9.9	1278	12.8	11.1
	Glacier de Leschaux (Mer de Glace)	Valley Glacier	45.89	6.96	9.6	1581	16.1	9.7
	Glacier d'Argentière	Valley Glacier	45.95	6.98	9.0	1469	15.5	14.9
	Unteraargletscher	Valley Glacier	46.56	8.19	8.9	692	7.3	6.0
	Glacier de Tré-La-tête	Valley Glacier	45.78	6.78	6.5	1237	15.4	11.4
Caucasus	Karagom Glacier	Valley Glacier	42.80	43.72	9.9	1904	19.2	17.2
	Tcey Glacier	Valley Glacier	42.75	43.84	6.2	1399	17.8	14.1
	Aylata Glacier	Valley Glacier	42.95	43.22	5.6	1058	14.2	12.3
	Bartuy Glacier	Valley Glacier	42.83	43.62	4.4	980	14.8	10.0
	Songuti Glacier	Valley Glacier	42.81	43.81	4.3	1156	17.7	11.5
Tibetan Plateau / Kunlun Mtns. / Qilian Mtns.	Guliya Ice Cap	Ice Cap	35.30	81.46	10.4	764	7.8	6.1
	Puruogangri Ice Cap	Ice Cap	33.91	89.14	8.0	591	6.7	5.4
	Dunde Ice Cap	Ice Cap	38.09	96.43	3.4	498	8.2	7.1
	West Kunlun Shan Glacier Complex	Icefield	35.35	80.96	18.0	932	6.9	6.1
	Monuomaha	Icefield	36.03	90.96	7.9	603	7.4	6.1
	Geladandong	Icefield	33.41	91.13	6.8	469	5.8	5.0
	Gaergangri–Gaqiadirugang Complex	Icefield	33.46	90.88	5.2	435	6.1	5.0

	Malan	Icefield	35.82	90.70	4.5	408	6.2	5.3
	Jinyang Gangri	Icefield	35.61	89.74	4.3	425	6.5	5.7
	—	Icefield	33.41	91.53	4.2	407	6.3	5.5
	Kangzhagri	Icefield	35.56	89.58	3.8	416	6.8	6.2
	—	Icefield	33.93	90.68	3.6	373	6.5	5.7
	Dongkemadi	Icefield	33.11	92.06	3.6	355	6.1	5.2
	Shulenanshan Glacier Complex	Icefield	38.48	97.73	2.9	414	7.3	6.2
	—	Icefield	36.12	90.11	2.7	379	7.4	6.3
	—	Icefield	35.82	91.94	2.5	321	6.5	5.7
	—	Icefield	35.88	91.45	2.5	373	7.6	6.7
	—	Valley Glacier	38.19	96.18	5.8	480	6.3	5.5
	—	Valley Glacier	38.20	96.14	5.5	411	5.6	4.7
	—	Valley Glacier	38.19	96.28	5.5	472	6.4	5.9
	—	Valley Glacier	36.59	91.16	5.3	390	5.4	4.7
	—	Valley Glacier	38.20	96.22	4.4	380	5.7	4.8
	—	Valley Glacier	38.53	97.86	4.2	399	6.1	5.3
	—	Valley Glacier	38.71	97.24	4.2	412	6.4	5.6
	—	Valley Glacier	38.73	97.19	3.9	386	6.2	5.0
	—	Valley Glacier	38.20	96.12	3.8	329	5.3	4.4
	—	Valley Glacier	36.61	91.21	3.8	335	5.5	4.9
	—	Valley Glacier	38.19	96.33	3.1	413	7.4	6.6
	—	Valley Glacier	36.23	91.95	2.7	300	5.9	4.8
	—	Valley Glacier	38.21	96.01	2.1	274	5.9	5.0
	—	Valley Glacier	38.23	96.10	2.1	288	6.2	5.9
	—	Valley Glacier	38.19	96.39	1.8	259	6.2	5.4
	—	Valley Glacier	38.19	96.36	1.8	280	6.7	6.1
	—	Valley Glacier	38.74	97.23	1.6	221	5.5	4.6
	—	Valley Glacier	38.37	95.93	1.3	337	9.3	7.5
	—	Valley Glacier	38.38	95.88	1.0	304	9.5	7.7
	—	Valley Glacier	38.38	95.90	0.9	295	9.9	8.6
	—	Valley Glacier	38.37	95.94	0.9	312	10.6	8.1
Tien Shan	North Inylchek Glacier	Valley Glacier	42.23	79.97	52.7	1603	7.0	4.5
	South Inylchek Glacier	Valley Glacier	42.16	80.11	49.6	1738	7.8	5.6
	Tuomur Glacier	Valley Glacier	41.89	79.95	30.8	1689	9.6	7.8
	Karagul Glacier	Valley Glacier	42.26	80.46	27.9	1397	8.4	6.8
	Tugbelchi Glacier	Valley Glacier	42.17	80.41	25.9	1410	8.7	6.5
	Muzart Glacier	Valley Glacier	42.32	80.83	24.6	1164	7.4	6.1
	Kayndy Glacier	Valley Glacier	42.09	79.71	23.3	1220	8.0	6.2
	Mushketova Glacier	Valley Glacier	42.29	79.90	19.5	1020	7.3	5.2
	Qong-Tailan Glacier (West)	Valley Glacier	41.92	80.20	18.0	1387	10.3	7.4
	Semenov Glacier	Valley Glacier	42.33	80.02	14.5	824	6.8	5.6
	Keqike-Tailan Glacier (West)	Valley Glacier	42.02	80.37	13.4	943	8.1	5.8
	Ayransu Glacier	Valley Glacier	41.91	79.82	12.9	1275	11.2	8.1
	Qong-Tailan Glacier (East)	Valley Glacier	41.98	80.26	12.2	1004	9.0	6.3
	Kolpakovsky Glacier	Valley Glacier	42.08	78.28	11.1	961	9.1	8.2
	Qong-Kozibai	Valley Glacier	42.00	80.60	11.0	803	7.6	6.2
	Keqike-Tailan Glacier (East)	Valley Glacier	41.98	80.48	9.4	1483	15.2	9.9
	North Karasai Glacier	Valley Glacier	41.80	78.23	8.4	673	7.3	5.8
	Dzhamasu Glacier	Valley Glacier	41.90	78.36	8.3	802	8.8	7.0
	Metallurg Glacier	Valley Glacier	42.15	78.49	6.0	673	8.7	7.8
	East Boroko Glacier	Valley Glacier	42.12	78.38	5.9	657	8.5	7.6
	Dzhangarttinbashi Glacier	Valley Glacier	41.64	78.90	5.9	561	7.3	6.0
	Kotortor (South) Glacier	Valley Glacier	42.04	78.20	5.6	416	5.5	5.0
	Kayndy Glacier (Ak-Shirak Range)	Valley Glacier	41.78	78.32	5.6	581	7.7	5.6
	—	Valley Glacier	42.33	79.81	5.4	686	9.3	7.4
	Saiktor Glacier	Valley Glacier	41.72	79.10	5.2	491	6.8	5.4

	—	Valley Glacier	42.33	79.84	5.2	671	9.3	7.3
	East Kiche Bordu Glacier	Valley Glacier	42.14	78.45	5.0	991	14.0	10.5
	Chuloktor Glacier	Valley Glacier	41.70	79.02	4.8	654	9.4	8.3
	—	Valley Glacier	42.04	78.17	4.8	487	7.1	6.0
	—	Valley Glacier	42.33	79.88	4.4	571	8.6	7.0
	Kichik Saiktor Glacier	Valley Glacier	41.71	79.05	4.3	521	7.9	6.4
	East Ontor Glacier	Valley Glacier	42.19	78.48	4.3	782	12.0	9.1
	—	Valley Glacier	41.66	78.93	4.2	484	7.4	6.7
	South Bordu Glacier	Valley Glacier	41.79	78.15	4.1	537	8.3	6.9
	West Kiche Bordu Glacier	Valley Glacier	42.14	78.43	3.9	836	13.3	11.2
	—	Valley Glacier	42.32	79.94	3.7	586	9.7	7.8
	—	Valley Glacier	42.32	79.91	3.6	520	8.7	7.2
Himalaya	Kanchenjunga Glacier	Valley Glacier	27.78	88.13	21.2	1319	9.1	5.8
	Zemu Glacier	Valley Glacier	27.74	88.25	20.1	1031	7.3	6.1
	Gyabrag Glacier	Valley Glacier	28.17	86.58	18.0	1117	8.2	5.2
	Kangshung Glacier	Valley Glacier	27.98	87.02	16.7	1131	8.8	6.8
	Yarlung Glacier	Valley Glacier	27.62	88.06	16.5	981	7.6	5.0
	Nangpa-Lunag Glacier	Valley Glacier	28.01	86.57	15.0	836	6.8	4.1
	Ngozumpa Glacier	Valley Glacier	28.00	86.69	14.1	1029	8.7	4.6
	Gyachung Kang Glacier	Valley Glacier	28.15	86.75	13.2	1112	9.7	6.8
	—	Valley Glacier	28.25	86.28	12.4	934	8.3	5.1
	Khumbu Glacier	Valley Glacier	27.98	86.83	12.3	1193	10.7	5.1
	—	Valley Glacier	28.45	85.57	11.3	825	7.8	5.1
	Daqu Glacier	Valley Glacier	28.44	85.70	11.2	724	6.8	4.4
	—	Valley Glacier	28.25	86.39	11.2	855	8.1	4.9
	—	Valley Glacier	28.34	86.36	10.1	883	8.8	6.4
	—	Valley Glacier	27.91	88.92	9.6	1102	11.2	8.6
	—	Valley Glacier	28.50	85.53	8.8	902	9.6	6.2
	—	Valley Glacier	28.26	86.22	8.2	718	7.9	5.1
	—	Valley Glacier	28.36	85.16	8.2	785	8.7	6.7
	—	Valley Glacier	28.58	85.44	7.6	852	9.7	5.6
	—	Valley Glacier	28.14	85.83	6.7	1411	17.2	14.9
	—	Valley Glacier	27.87	88.91	6.7	603	7.4	6.8
	—	Valley Glacier	27.87	88.82	6.7	1091	13.4	6.4
	—	Valley Glacier	28.31	85.14	6.6	1219	15.0	10.0
	—	Valley Glacier	28.36	86.42	6.4	773	9.6	8.0
	—	Valley Glacier	28.35	86.39	5.8	650	8.5	7.2
	—	Valley Glacier	28.34	86.27	5.5	465	6.3	5.3
	—	Valley Glacier	28.65	85.40	5.3	547	7.5	5.6
	—	Valley Glacier	28.56	85.40	5.3	635	8.7	6.4
	—	Valley Glacier	28.42	85.14	5.0	1288	18.3	10.6
	—	Valley Glacier	28.54	85.37	4.8	902	13.0	8.6
	—	Valley Glacier	28.36	86.44	4.5	556	8.3	6.8
	—	Valley Glacier	27.98	88.25	4.3	625	9.5	6.9
	—	Valley Glacier	28.37	86.45	4.2	585	9.0	6.9
	—	Valley Glacier	28.33	86.23	4.1	445	7.0	4.6
	—	Valley Glacier	28.58	85.47	4.1	647	10.1	7.0
	—	Valley Glacier	27.97	88.20	3.8	405	6.6	6.0
	—	Valley Glacier	28.57	85.35	3.6	454	7.5	6.6
	—	Valley Glacier	28.37	86.46	3.1	466	8.3	6.3
	—	Valley Glacier	28.70	85.44	2.7	606	11.6	8.7
	—	Valley Glacier	28.38	86.47	2.6	384	7.5	6.4

Table 2. Palaeo ice masses in published reconstructions, and parameters L, C^* and $\tilde{C}$ for their surface profiles. Entries are ordered by decreasing span (L). Shaded entries have $\tilde{C} < \tilde{C}_{MIN}$. Methods in column four are: 1 = Hand drawing (observing geomorphic constraints and using modern ice masses as analogues), 2 = iterative flowline modelling, 3 = glacio-isotatic numerical inversion, 4 = three-dimensional thermo-mechanically coupled numerical ice sheet model, 5 = parabolic profiling.

No.	Location	Ice mass	Reconstruction method	Span, L (km)	C^* ($m^{1/2}$)	$\tilde{C}$ ($m^{1/2}$)	Reference
1	North America	Laurentide Ice Sheet	5	1970	2.4	2.4	CLIMAP (1981)
2	North America	Laurentide Ice Sheet	5	1510	2.4	2.3	Dyke et al. (2002); modified by Winsborrow (2007)
3	Isle of Mull, Scotland	Mull Icefield	1	9.8	4.5	4.0	Ballantyne (2002)
4	West Drumochter Hills, Scotland	Drumochter Icefield	1	7.2	4.5	3.9	Benn and Ballantyne (2005)
5	North Harris, Outer Hebrides, Scotland	Glen Langdale Glacier	1	7.0	3.9	3.5	Ballantyne (2007a)
6	North Harris, Outer Hebrides, Scotland	Glen Meavaig Glacier	1	5.5	3.1	2.8	Ballantyne (2007a)
7	North Harris, Outer Hebrides, Scotland	Glen Ulladale Glacier	1	4.4	3.9	3.5	Ballantyne (2007a)
8	North Harris, Outer Hebrides, Scotland	Gleann Bearraray Glacier	1	1.3	4.2	3.8	Ballantyne (2007a)
9	North Harris, Outer Hebrides, Scotland	Gleann Dubh Glacier	1	1.3	3.8	3.5	Ballantyne (2007a)
10	North Arran, Scotland	Tanna Glacier	1	1.2	2.4	2.3	Ballantyne (2007b)
	North America	Laurentide Ice Sheet	3	1610	2.9	2.6	Peltier (2004)
	British Isles	British Isles Ice Sheet	4	365	2.8	2.7	Boulton and Hagdorn (2006)
	Montana, USA	Ice cap	2	88	4.0	3.8	Locke (1995)
	Northern Scandinavia	Icefield	2	63	5.8	6.0	Fredin (2004; Figs. 4 and 5)
	Colorado, USA	Taylor River Glacier Complex	1	12.0	6.7	5.5	Brugger (2006)
	Isle of Skye, Scotland	Cullin Icefield	1	9.6	5.6	5.1	Ballantyne (1989)
	Venezuelan Andes	Mucubaji	1	9.2	11.8	8.9	Stansell et al. (2007)
	Isle of Skye, Scotland	Glacier 9	1	9.0	10.3	8.8	Ballantyne (1989)
	Venezuelan Andes	Negra	1	8.7	14.0	10.4	Stansell et al. (2007)
	North Norway	Plateau Icefield	2	8.5	11.6	10.0	Rea and Evans (2007)
	Western Mexico	glacier at (19º 24.5', –102º 19')	1	6.5	7.7	6.8	Lachniet and Vazquez-Selem (2005)
	Venezuelan Andes	Michurao	1	6.2	8.3	7.2	Stansell et al. (2007)
	Western Mexico	glacier at (19º 26', –102º 19')	1	5.9	6.8	5.8	Lachniet and Vazquez-Selem (2005)
	Serra da Estrela, Portugal	Plateau Icefield	2	5.6	13.0	11.9	Vieira (2008)
	Venezuelan Andes	Cerros Los Pantanos	1	5.3	9.6	8.3	Stansell et al. (2007)
	English Lake District	Glacier 7	1	4.9	9.1	7.4	Sissons (1980)
	Western Mexico	glacier at (19º 26', –102º 20.5')	1	4.9	7.5	7.0	Lachniet and Vazquez-Selem (2005)
	Venezuelan Andes	El Balcon	1	4.9	7.1	6.1	Stansell et al. (2007)
	Venezuelan Andes	Granates	1	4.7	9.5	8.8	Stansell et al. (2007)
	English Lake District	Plateau Icefield	1	4.6	9.5	8.1	McDougall (2001)
	English Lake District	Glacier 9	1	4.5	9.6	7.9	Sissons (1980)
	Venezuelan Andes	Llano del Trigo	1	4.4	10.6	9.1	Stansell et al. (2007)
	Venezuelan Andes	Filo Los Pantanos	1	4.4	7.5	6.5	Stansell et al. (2007)
	Isle of Mull, Scotland	Corrie Glacier 5	1	4.1	9.0	7.5	Ballantyne (2002)
	Isle of Skye, Scotland	Glacier 6	1	4.0	10.4	8.6	Ballantyne (1989)
	Western Mexico	glacier at (19º 26', –102º 19.8')	1	3.5	10.9	9.6	Lachniet and Vazquez-Selem (2005)

English Lake District	Glacier 2	1	3.4	5.3	5.2	Sissons (1980)
Isle of Mull, Scotland	Corrie Glacier 4	1	3.3	8.8	7.3	Ballantyne (2002)
Western Mexico	glacier at (19º 25', –102º 21')	1	3.3	6.6	5.8	Lachniet and Vazquez-Selem (2005)
Venezuelan Andes	Las Viraviras	1	3.3	5.2	4.6	Stansell et al. (2007)
English Lake District	Glacier 6	1	3.1	13.4	9.8	Sissons (1980)
North Harris, Outer Hebrides, Scotland	Glen Scaladale Glacier	1	3.0	6.6	5.5	Ballantyne (2007a)
North Arran, Scotland	Glen Catacol Glacier	1	3.0	6.3	5.9	Ballantyne (2007b)
Island of Rhum, Scotland	Glacier 9	1	2.8	8.7	7.6	Ballantyne and Wain-Hobson (1980)
Island of Rhum, Scotland	Glacier 5	1	2.8	7.8	7.0	Ballantyne and Wain-Hobson (1980)
English Lake District	Glacier 3	1	2.8	6.6	6.4	Sissons (1980)
Isle of Skye, Scotland	Glacier 5	1	2.6	11.2	9.6	Ballantyne (1989)
Isle of Skye, Scotland	Glacier 10	1	2.6	7.3	6.8	Ballantyne (1989)
Isle of Skye, Scotland	Glacier 2	1	2.5	13.6	11.4	Ballantyne (1989)
Western Mexico	glacier at (19º 24.5', –102º 21')	1	2.5	7.9	7.5	Lachniet and Vazquez-Selem (2005)
English Lake District	Glacier 10	1	2.4	13.0	11.9	Sissons (1980)
Isle of Skye, Scotland	Glacier 3	1	2.4	12.5	10.4	Ballantyne (1989)
Isle of Skye, Scotland	Glacier 4	1	2.4	12.2	10.7	Ballantyne (1989)
North Arran, Scotland	Glen Sannox Glacier	1	2.4	9.4	8.5	Ballantyne (2007b)
Isle of Mull, Scotland	Corrie Glacier 6	1	2.3	5.0	4.5	Ballantyne (2002)
Island of Rhum, Scotland	Glacier 7	1	2.2	9.1	8.5	Ballantyne and Wain-Hobson (1980)
Isle of Mull, Scotland	Corrie Glacier 2	1	2.1	6.7	5.5	Ballantyne (2002)
English Lake District	Glacier 4	1	2.0	7.8	7.1	Sissons (1980)
Western Mexico	glacier at (19º 24.5', –102º 20')	1	1.9	9.3	8.2	Lachniet and Vazquez-Selem (2005)
North Arran, Scotland	Glen Lorsa Glacier	1	1.9	6.5	6.0	Ballantyne (2007b)
North Arran, Scotland	Gleann Easan Biorach Glacier	1	1.9	5.6	5.6	Ballantyne (2007b)
North Arran, Scotland	Glen Rosa Glacier	1	1.8	10.1	8.5	Balantyne (2007b)
Western Mexico	glacier at (19º24.5', –102º20.5')	1	1.8	8.0	6.9	Lachniet and Vazquez-Selem (2005)
English Lake District	Glacier 1	1	1.8	7.1	6.9	Sissons (1980)
English Lake District	Glacier 5	1	1.8	5.4	5.5	Sissons (1980)
Isle of Skye, Scotland	Glacier 8	1	1.6	7.3	5.9	Ballantyne (1989)
North Harris, Outer Hebrides, Scotland	Glen Skeaudale Glacier	1	1.6	5.5	5.1	Ballantyne (2007a)
Isle of Skye, Scotland	Glacier 1	1	1.5	13.7	11.5	Ballantyne (1989)
North Arran, Scotland	Coire a'Bhradain Glacier	1	1.5	7.9	6.8	Ballantyne (2007b)
Isle of Skye, Scotland	Glacier 7	1	1.4	12.6	12.1	Ballantyne (1989)
English Lake District	Glacier 8	1	1.4	7.6	6.8	Sissons (1980)
Isle of Mull, Scotland	Corrie Glacier 1	1	1.3	7.6	6.9	Ballantyne (2002)
North Harris, Outer Hebrides, Scotland	Cleister Glacier	1	1.2	8.1	7.8	Ballantyne (2007a)
North Harris, Outer Hebrides, Scotland	Coire Dubh Glacier	1	1.2	7.3	6.7	Ballantyne (2007a)
North Harris, Outer Hebrides, Scotland	An Coire Glacier	1	1.1	8.9	8.0	Ballantyne (2007a)
North Arran, Scotland	Coire nan Ceum Glacier	1	1.1	8.6	7.4	Ballantyne (2007b)
North Arran, Scotland	Garbh Choire Glacier	1	1.1	6.8	5.9	Ballantyne (2007b)
Isle of Mull, Scotland	Corrie Glacier 3	1	1.1	6.1	5.5	Ballantyne (2002)
Island of Rhum, Scotland	Glacier 8	1	0.9	6.5	5.9	Ballantyne and Wain-Hobson (1980)
Island of Rhum, Scotland	Glacier 3	1	0.8	5.8	5.6	Ballantyne and Wain-Hobson (1980)
North Arran, Scotland	Ealta Choire Glacier	1	0.7	7.5	7.0	Ballantyne (2007b)
Island of Rhum, Scotland	Glacier 4	1	0.7	5.4	5.0	Ballantyne and Wain-Hobson (1980)
Island of Rhum, Scotland	Glacier 2	1	0.6	6.1	5.5	Ballantyne and Wain-Hobson (1980)
Island of Rhum, Scotland	Glacier 1	1	0.6	7.2	6.2	Ballantyne and Wain-Hobson (1980)
Island of Rhum, Scotland	Glacier 10	1	0.6	7.5	6.4	Ballantyne and Wain-Hobson (1980)
Island of Rhum, Scotland	Glacier 6	1	0.5	6.3	5.9	Ballantyne and Wain-Hobson (1980)